FACILE SYNTHESIS OF BIMETALLIC NANOPARTICLES WITH DIVERSE NANOSTRUCTURES USING METAL ACETYLACETONATES

A THESIS SUBMITTED TO

THE GRADUATE SCHOOL OF ENGINEERING AND SCIENCE

OF BILKENT UNIVERSITY

IN PARTIAL FULFILLMENT OF THE REQUIREMENTS FOR

THE DEGREE OF

MASTER OF SCIENCE

IN

MATERIALS SCIENCE AND NANOTECHNOLOGY

By

Dalya M. F. Sayma

January 2024

FACILE SYNTHESIS OF BIMETALLIC NANOPARTICLES WITH DIVERSE NANOSTRUCTURES USING METAL ACETYLACETONATES

By Dalya M. F. Sayma

January 2024

We certify that we have read this thesis and that in our opinion it is fully adequate, in scope and in quality, as a thesis for the degree of Master of Science.

Wonmi Ahn (Advisor)

Ferdi Karadaş

Ekin Aslan

Approved for the Graduate School of Engineering and Science:

Orhan Arıkan
Director of the Graduate School

ABSTRACT

FACILE SYNTHESIS OF BIMETALLIC NANOPARTICLES WITH DIVERSE NANOSTRUCTURES USING METAL ACETYLACETONATES

Dalya Sayma
M.S. in Materials Science and Nanotechnology
Advisor: Wonmi Ahn
January 2024

Bimetallic nanoparticles (NPs) have become a fundamental subject in the field of nanoscience and inorganic chemistry. Owing to the fascinating optical and catalytic properties that rise from their synergetic effect, plasmonic-catalytic bimetallic NPs, in particular, are employed in a myriad of applications such as catalysis, sensing and photocatalysis. Optical properties of plasmonic NPs such as gold or silver NPs are based on the localized surface plasmon resonance (LSPR) in the visible spectral range. Plasmonic NPs enhance the localization of electromagnetic fields, converting light to hot carriers or heat that can be used to drive chemical reactions. On the other hand, catalytic metals, which have d-bands close to the Fermi-level, make strong binding to reactants and lower the activation energy of chemical reactions. The properties of plasmonic-catalytic bimetallic NPs such as efficiency or product selectivity in the chemical reaction do not only rely on factors like size and composition of metal NPs, but more importantly, on the types of nanostructures formed. Herein, several nanostructures were synthesized by developing a facile approach using metal acetylacetonates. The synthesized NPs include bare silver NPs, bare palladium NPs, Pd@Ag core-shell NPs, Pd@Ag nanowires, Ag-Pd alloyed core-satellite NPs, Ag-Pt alloyed nano-stars and concave nano-cubes, and trimetallic AgPdPt NPs. In this study, it was found that the temperature, composition of metal components, and amount of capping and reducing agents play a key role in the synthesis of different types of bimetallic NPs. This study is important in the field of nanochemistry as it provides a novel synthesis method for generating plasmonic-catalytic bimetallic NPs.

Keywords: Bimetallic nanoparticles, Silver, Palladium, Platinum, Alloy, Plasmonic, Nanocatalyst, Core-satellite

ÖZET

METAL ASETLACETONATLAR KULLANILARAK ÇETL NANO YAPILARA SAHP BMETALK NANOPARÇACIKLARIN KOLAY SENTEZ

Dalya Sayma
Malzeme Bilimi ve Nanoteknoloji, Yüksek Lisans
Tez Danışmanı: Wonmi Ahn
January 2024

Bimetalik nanopartiküller (NP'ler), nanobilim ve inorganik kimya alanında temel bir konu haline gelmiştir. Sinerjik etkilerinden kaynaklanan büyüleyici optik ve katalitik özellikler nedeniyle, özellikle plazmonik-katalitik bimetalik NP'ler, kataliz, algılama ve fotokataliz gibi sayısız uygulamada kullanılır. Altın veya gümüş NP'ler gibi plazmonik NP'lerin optik özellikleri, görünür spektral aralıktaki lokalize yüzey plazmon rezonansına (LSPR) dayanmaktadır. Plazmonik NP'ler, ışığı sıcak taşıyıcılara veya kimyasal reaksiyonları yönlendirmek için kullanılabilecek ısıya dönüştürerek elektromanyetik alanların lokalizasyonunu artırır. Öte yandan Fermi düzeyine yakın d-bantlarına sahip katalitik metaller, reaktanlara güçlü bağlanma yaparak kimyasal reaksiyonların aktivasyon enerjisini düşürür. Plazmonik-katalitik bimetalik NP'lerin kimyasal reaksiyondaki verimlilik veya ürün seçiciliği gibi özellikleri yalnızca metal NP'lerin boyutu ve bileşimi gibi faktörlere değil, daha da önemlisi oluşan nanoyapı türlerine de bağlıdır. Burada metal asetilasetonatlar kullanılarak kolay bir yaklaşım geliştirilerek çeşitli nanoyapılar sentezlendi. Sentezlenen NP'ler çıplak gümüş NP'leri, çıplak paladyum NP'leri, Pd@Ag çekirdek-kabuk NP'lerini, Pd@Ag nanotellerini, Ag-Pd alaşımlı çekirdek-uydu NP'lerini, Ag-Pt alaşımlı nanoyıldızları ve içbükey nano-küpleri ve trimetalik AgPdPt'yi içerir. NP'ler. Bu çalışmada, farklı türdeki bimetalik NP'lerin sentezinde sıcaklığın, metal bileşenlerin bileşiminin, kaplama ve indirgeyici ajanların miktarının önemli bir rol oynadığı bulunmuştur. Bu çalışma, plazmonik-katalitik bimetalik NP'lerin üretilmesi için yeni bir sentez yöntemi sağladığından nanokimya alanında önemlidir.

Anahtar sözcükler: Bimetalik nanopartiküller, Gümüş, Paladyum, Platin,

Alaşım, Plazmonik, Nanokatalizör, Çekirdek uydu..

Acknowledgement

I would like to thank my advisor, Dr. Wonmi Ahn, for her support, guidance, and mentorship throughout this research. Her encouragement and insightful feedback have played a role in shaping the quality of this thesis. I am also profoundly thankful to my thesis committee members for their constructive comments and suggestions. Additionally, I would like to thank my parents and siblings for their support, as their continuous encouragement has been a source of strength for me. Special thanks to Dr. Süleyman Tekmen and Eng. Mustafa Güler for taking TEM imaging for my samples as they were flexible and cooperative. Their expertise has significantly improved the quality of my results . Lastly, I would like to thank all my friends for their support throughout my time in Bilkent.

Contents

List of Figures

List of Tables

Chapter 1

Introduction

Bimetallic nanoparticles have attracted researchers in a variety of applications. Bimetallic nanoparticles are a combination of two metal elements with enhanced properties and characteristics that may significantly modify and enhance nanoparticles' stability, activity, or selectivity in catalysis, due to their synergetic effect [1][2]. Fig.1.1 shows different groups of metals that have distinguished properties, such as magnetic metals (Fe, Co, Ni), plasmonic metals (Cu, Au, Ag), and catalytic metals (Pd, Pt, Rh, Ru, Ir) [3].

The structure of bimetallic nanoparticles relies on the distribution of both elements, where they could be distributed forming solid solution alloy, intermetallic alloy, core-shell, heterostructure, or other nanostructures. Mono-metallic NPs can have octahedrons, decahedrons, cubes, concave cubes, rods, or other simple shapes. However, combining two metals allows more possibilities for more complex shape formation due to the various distributions of every metal in the particle (Fig1.2) [4]. Some questions should be considered before designing bimetallic nanoparticles: How will the composition and structure of bimetallic nanoparticles designed affect their optical properties? What are the effects of the synthesis methods and conditions of the reaction on their structure? What characteristics are significant for catalysis or photocatalysis? [4]

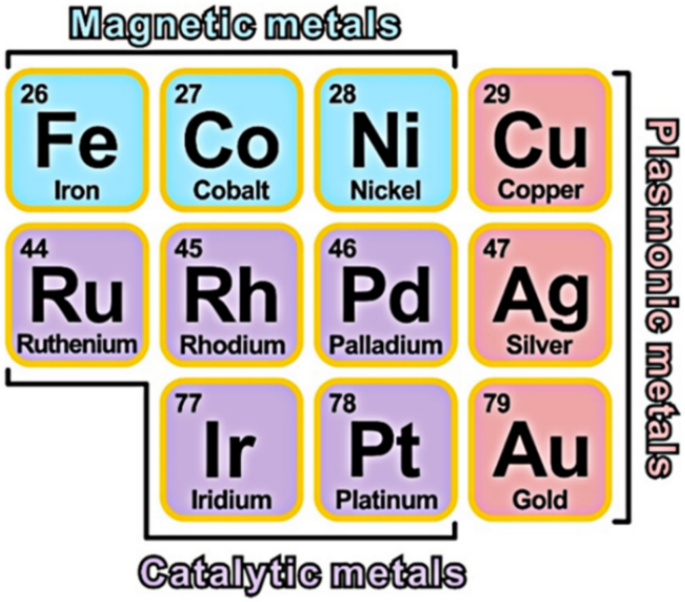

Figure 1.1: A section of the periodic table delineating the distinctive properties of each element. Reprinted with permission from ref [17]. Copyright 2016 American Chemical Society.

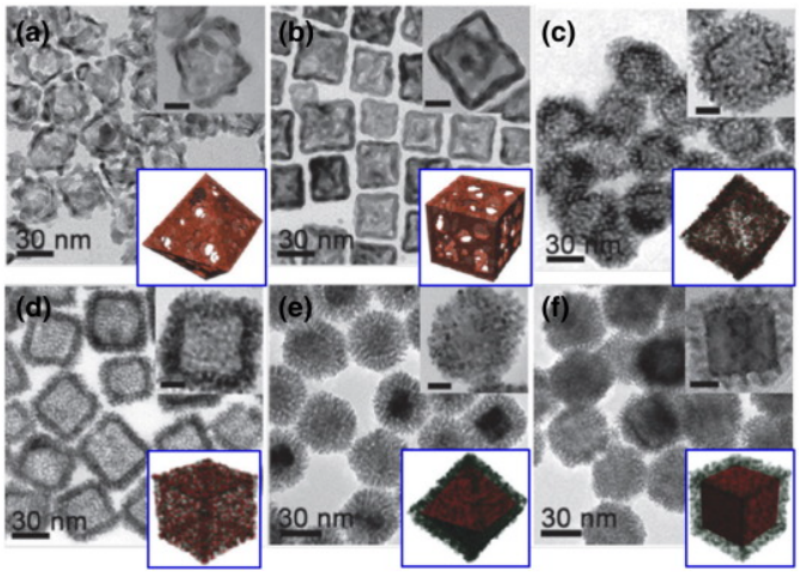

Figure 1.2: TEM images for bimetallic nanoparticles with different nanostructures: (a) PtPd alloy forming octahedral nanocages,(b) PtPd alloy forming cubic nanocages, (c) PtPd alloy octahedral with a dendritic hollow structure, (d) PtPd alloy with cubic dendritic hollow structure (e) Pd@Pt core–shell forming cubic dendritic structure, and (f) Pd@Pt core–shell with a cubic dendritic structure Reprinted with permission from ref [5]. Copyright 2016 American Chemical Society..

1.1 Electronic Properties of Plasmonic and Catalytic Metals

Some metal nanoparticles are plasmonic, supporting localized surface plasmon resonance (LSPR), transforming incident light to hot carriers or heat, to drive chemical reactions [6]. Other metals are known for their catalytic properties, showing enhanced chemisorption for facilitating the chemical reaction.

Plasmonic and catalytic metals have significant differences in their electronic structure, as each has a phenomenon absent in the other. Plasmonic metals are known to have the d-bands far away from the Fermi- level, which leads to intraband transitions. Catalytic metals, on the other hand, have d-bands close to the Fermi level. This dampens (LSPR) due to interband transitions dominating the optical response (Fig.1.3 a-b). The simulated optical response was compared between plasmonic or catalytic metals for a 20 nm nanoparticle. Ag shows the highest extinction cross-section among other plasmonic metals as its d-band is the furthest from the Fermi level. On the other hand, catalytic metals show weak optical response in the visible range (Fig.1.3 c).

When the molecular adsorbate binds on the catalytic material, it forms bonding and antibonding states, where bonding states are fully occupied, and antibonding states are not populated due to their higher energy as they are lying above the Fermi-level [7]. In transition metals, when a molecule is adsorbed on the metal's surface, it interacts with both sp and d bands, where the sp band renormalizes the molecular orbitals; the highest occupied molecular orbital (HOMO) and lowest unoccupied molecular orbital (LUMO). As a result, the d-band determines the catalytic adsorption rate according to its proximity from the Fermi level. This explains why plasmonic metals are unsuitable catalytic materials due to the deep-lying existence of the d-band from the Fermi level.

However, strong chemisorption is also undesired. Reactants need to bond to the catalyst's surface for the reaction to proceed, allowing for product desorption. For strong chemisorption, hindering the removal of products from the catalyst's

surface will poison the catalyst, preventing other reactants from binding and other reactions from proceeding. This chemisorption behavior is demonstrated by Sabatier's principle, which claims that chemisorption should be strong enough for the reaction to proceed but not too strong to prevent desorption. Fig.1.3d shows a volcano plot demonstrating Sabatier's principle, where the right side of the volcano plot represents a strong binding of reactants to the catalyst surface which makes desorption difficult, and so the reaction is desorption limited. The left side of the plot, however, is adsorption limited, where reactans weakly get adsorbed on the catalyst surface and require high temperatures. The summit of the plot is the one that provides the minimum temperature for binding of the reactants and provides a balance between adsorption and desorption rates, which is the optimal case. Catalytic elements, such as palladium or platinum, are positioned near the peak of the volcano plot, and are used interchangeably in a combination with the plasmonic metal (Ag) in our study, in order to provide both optical and catalytic properties of our bimetallic nanoparticles, with a defined nanostructure.

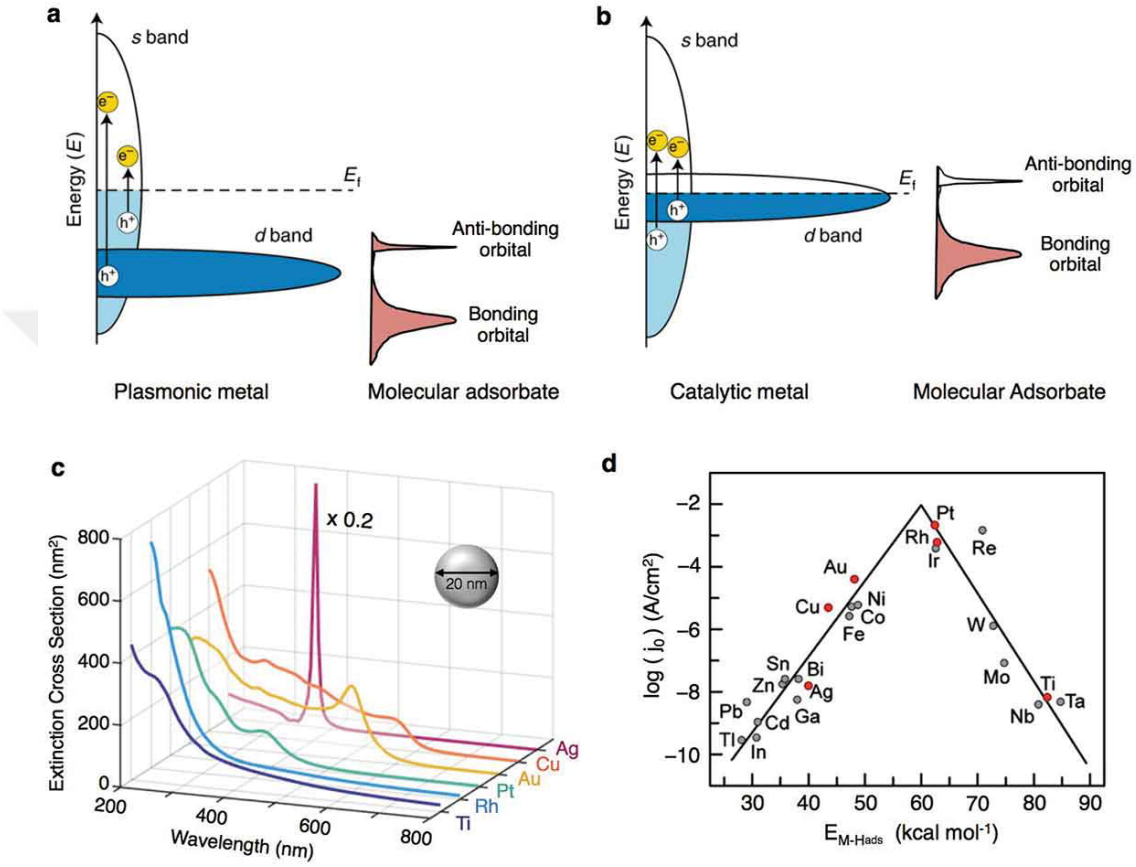

Figure 1.3: Electronic properties of plasmonic and catalytic metals. (a,b) Electronic band structure for plasmonic and catalytic metals, respectively, with the density of states (DOS) of a simple molecular adsorbate on the right of each diagram (c) Simulated extinction cross-sections of a 20 nm nanoparticle in water for a variety of plasmonic and catalytic metals. To fit in the same graph, the Ag optical response is multiplied by 0.2. (d) Volcano plot of the hydrogen evolution reaction (HER) for various metal electrodes in acidic media. The metals plotted in red represent the metals denoted in (c). (Figure adapted from [6]).

1.2 Types of Bimetallic NPs

Bimetallic nanostructures can be mainly categorized depending on the atomic ordering and configuration of the two metal components: alloys (intermetallic or solid solution), core-shell, or heterostructure. Other derivatives would include core frames, nanocages, etc. According to the metal precursors and synthesis conditions, different crystal facets can be formed, including low or high Miller indices surfaces or a mix of both. Bimetallic nanostructures can be 0-D, 1-D, or 2-D. A zero-dimensional nanostructure can expand in all three dimensions, such as polyhedrons. A one-dimensional nanostructure indicates the extension of one dimension, including nanowires, nanorods, etc. A 2-dimension nanostructure indicates the expansion in 2 dimensions, such as nanosheets, nanoplates, and so on [3].

1.2.1 Alloyed Nanostructure

It is known that alloyed materials show distinct physicochemical properties. Alloys are homogeneous mixtures with particular atom arrangement, with metal bonding between both metals present within the bimetallic alloy. Based on atomic arrangement, alloys can be classified into solid solutions or intermetallic compounds. A solid solution alloy has the atoms randomly distributed within the alloy. On the other hand, an intermetallic alloy has atoms distributed in an arranged atomic order. The co-reduction method is usually used for synthesizing a bimetallic solid-solution alloy, where it is difficult to control the atomic ordering as both metals are simultaneously reduced. For alloying two metals, A and B, there are three key factors to be met: (a) the A-B bond should be more robust than A-A and B-B bonds; (b) A and B bulk metals should have similar or close surface energies; and (c) close atomic sizes to enhance the alloying mechanism [8].

From a thermodynamic perspective, the atomic arrangement within a bimetallic alloy can be investigated by measuring the change in Gibbs free energy when

mixing under a particular condition. In an ideal binary system alloy, the Gibbs free energy of mixing (ΔG_{mix}) is given by the equation [9]:

$$\Delta G_{\text{mix}} = \Delta H_{\text{mix}} - T\Delta S_{\text{mix}}$$

where T is reaction temperature, ΔH_{mix} and $\text{T}\Delta S_{\text{mix}}$ represent the changes of enthalpy and entropy before and after the reaction, respectively. As a rule, the negative value of ΔG_{mix} means that both metals are soluble in each other.

1.2.2 Core-Shell Nanostructure

The core-shell structure is formed when metal A is coated with another metal, forming a low or high shell coverage [10]. In a one-pot synthesis step, when two metals have different reduction potentials, the metal with the highest reduction potential usually gets reduced first. Then, the lower potential metal gets reduced after that. Other factors in the reaction environment would change the reducing abilities of metals. For instance, in some reaction conditions, when a specific halide is introduced to the reaction, it increases the reduction potential of the metal that has a low reduction potential [11]. Another approach is seed-mediated growth, which proved to be an efficient method for synthesizing core-shell structures. The thickness of shell can be varied and controlled on the atomic level [12], depending on the reaction conditions, such as the amount of metal precursor.

1.2.3 Heterostructure

In a heterostructure, metal B has three growing possibilities on metal A: layer-layer, film-island, and island growth. When the bonding energy between A-A in metal A is higher than A-B, metal B grows in an island growth mode to reduce the lattice stress between metals A and B.

1.3 Synthesis Strategies of Bimetallic NPs

Since the properties of bimetallic nanoparticles depend on their size, composition, and shape, it is crucial to control them through the synthesis procedure. The synthesis of nanoparticles involves two steps: nucleation and growth. It is difficult to control these two stages' thermodynamic and kinetic processes as they are often continuous and cannot be separated easily. Many researchers have been investigating variations of metal precursors, reducing agents, temperature, capping agents, and time to control nucleation and growth of nanocrystals. As a result, many synthetic techniques have been developed, and some synthesis methods require combining more than one synthesis strategy. Herein, only the typical and most used synthesis strategies will be discussed: co-reduction, seed-mediated growth, thermal decomposition, and galvanic replacement [3].

1.3.1 Co-reduction

A co-reduction synthetic process is where two metals are simultaneously reduced. This method is quite simple for the synthesis of intermetallic compounds. Different structures can be produced according to the nature of the metal precursors used and the synthesis environmental conditions. For instance, metals with similar reduction potentials would result in an alloy [13]. On the other hand, metals with different reduction potentials would give a core-shell nanostructure, as the metal with the highest reduction ability will reduce first. Then, the metal with the lowest reducing ability will reduce later, forming a shell on the metal core that was first formed [14]. Co-reduction synthesis can be classified into solvothermal and oil-phase reduction methods depending on reaction conditions.

1.3.2 Seed-Mediated Growth

Seed-mediated growth is an effective strategy for controlling synthesis, especially for producing core-shell nanostructures, where seeds are first synthesized. The

other metal precursor is added and reduced as a shell in another synthesis step. The activation energy for nucleation is known to be higher than that for growth of a nanocrystal. Subsequently, a heterogeneous shell would form as the second metal tends to reduce, nucleate on some core sites, and grow on them. However, forming a homogeneous shell is more complex and depends on several factors, including the metal bonds, surface energy, and stabilizers used in the reaction [3].

1.3.3 Thermal Decomposition

Thermal decomposition involves heating organic compounds with low reduction potentials that tend to decompose and get reduced, forming nanocrystals. Generally, metal acetylacetonates can be reduced by thermal decomposition under moderate conditions. If two metals have different decomposition temperatures, thermal decomposition can be a strategy for core-shell formation in a one-pot synthesis method [15]. The metal with a lower decomposition temperature could be first reduced, and the temperature can be adjusted for the later reduction of the other metal with the higher decomposition temperatures, forming bimetallic core-shell nanostructures.

1.3.4 Galvanic Replacement Reaction (GRR)

Galvanic replacement reaction is an effective strategy for forming distinguished nanostructures, mainly based on both metals' reduction potentials [16]. It is considered an oxidation-reduction reaction, where one metal, acting as a template, undergoes oxidation by the ions of the other metal with a higher reduction potential.

Galvanic replacement reaction is propelled by the difference between the two elements involved. The change in Gibbs free energy ΔG is given by:

$$\Delta G = -nFE \tag{1.2}$$

where n represents the number of moles of electrons transferred in the half reaction, F denotes Faraday's constant, and E indicates the potential difference between two electrochemical reactions [17].

A positive potential difference gives a negative ΔG value, and so a spontaneous reaction. The potential difference can be demonstrated using the Nernst equation:

$$E = E^{\circ} - \frac{RT}{nF} \ln(Q) \tag{1.3}$$

where E° represents the standard potential difference at 25 °C, R denotes the ideal gas constant, T is the temperature, and Q represents the reaction quotient derived from concentration of products and reactants at a particular time.

1.4 Aim of The Study

This study aims to synthesize bimetallic NPs that combine plasmonic and catalytic properties. For instance, alloyed NPs can decrease the cost of the catalytic reaction with increasing the efficiency of the reaction due to synergetic effect [52]. Different nanostructures were synthesized for later use in different chemical reactions. Nanostructures with different shapes play a crucial role in the overall efficieny of chemical reactions. In this study, for instance, alloyed core-satellite nanostructures were synthesized that would increase the surface area for reactions. Ag-Pt alloyed NPs with nano-stars structure were synthesized as to facilitate mass transport of reactants and products. Also, perfectly spherical palladium NPs were synthesized. Perfectly spherical nanocrystals show different optical properties from faceted nanoparticles, especially when nanoparticles form dimers to generate surface plasmon coupling [42].

Chapter 2

Experimental Details and Characterization Techniques

2.1 Materials

Chemicals used for synthesis of mono and bimetallic nanoparticles were used as purchased without further purification, as listed in the table below:

Chemical Name	Supplier	Purity or other properties
Silver acetylacetonate (Ag(acac))	Sigma-Aldrich	99%
Palladium (II) acetylacetonate $Pd(acac)_2$	Sigma-Aldrich	98%
Platinum(II) acetylacetonate $Pt(acac)_2$	Sigma-Aldrich	97%
Polyvinylpyrrolidone (PVP)	Sigma-Aldrich	Molecular weight = 55,000
N,N-Dimethylmethanamide (DMF)	Sigma-Aldrich	
Ethanol	Sigma-Aldrich	99%
Acetone	Sigma-Aldrich	99.5%
Sodium Iodide (NaI)	Sigma-Aldrich	
DI water		Resistivity: 18.2 MΩ.cm

Table 2.1: Chemicals used in the synthesis of mono and bimetallic nanoparticles.

2.2 Synthesis of Monometallic, Bimetallic, and Trimetallic NPs

All glassware and teflon liner were cleaned with aqua-regia, ethanol, acetone, and DI water before use.

Metal(A)@Metal(B) refers to a core-shell structure, where the core is made up of metal A, and shell is made up of metal B.

Metal(A)@Metal(A)Metal(B) refers to a nanoparticle that has a core made up of metal A, and the shell is made up of an alloy(A and B).

2.2.1 Synthesis of Silver Nanoparticles

In a 100 ml rounded beaker, 300 mg of PVP were dissolved in 100 ml of nitrogen-saturated DI water. The solution was continuously stirred for 15 minutes. 100 mg of Ag(acac) were added to the solution with continuous stirring for 11 minutes at 2000 rpm, increased gradually to 3500 rpm. Then, the solution was placed in a water bath, with temperature maintained at 100 °C, heated for 12 min. The solution was cooled down to room temperature and then stored. Before use, colloidal NPs solution was washed with ethanol several times at 15000 rpm for 15 min. Silver NPs which yielded from this protocol were used as core NPs for the synthesis of AgPd core-satellite, AgPt, and AgPdPt alloyed NPs.

For samples synthesized via a dry bath, 2 mg of PVP was dissolved in 2 ml of nitrogen-saturated water in a vial. Then, 2 mg of Ag(acac) was added and stirred for 1 min. The vial was sealed and placed in oven at 50 °C. Same protocol was used for samples at 80 °C and 130 °C. As the samples were compared to the water-bath medium experiment in the discussion section, a sample with the same amount of material was prepared via water-bath medium for accuracy.

2.2.2 Synthesis of Palladium Nano-Cubes

Palladium nano-cubes were prepared according to a reported method [11]. In a typical synthesis, 50 mg of $Pd(acac)_2$, 160 mg of PVP, and 2 ml of NaI solution (0.15 g/mL) were mixed in 10 ml of DMF. The resulting light brown solution was then transferred to a teflon-lined stainless-steel autoclave. Then, the autoclave was heated at 150 °C for 8 h, cooled down to room temperature and the nanoparticles were washed in a 1:8 ethanol/acetone mixture several times at 5000 rpm for 5 min.

2.2.3 Synthesis of Palladium Spherical Nanoparticles

Palladium nano-cubes(25 mg), synthesized according to previous protocol, were washed with acetone/ethanol mixture and then were dispersed in 10 ml DMF. 160 mg of PVP, 25 mg of Ag(acac), and 2 ml of NaI solution (0.15 g/mL) were all added to the DMF solution, respectively. The resulting solution was then transferred to a teflon-lined stainless-steel autoclave. Then, the autoclave was heated at 150 °C for 8 h, cooled down to room temperature and the nanoparticles were washed in a 1:8 ethanol/acetone mixture several times at 5000 rpm for 5 min.

2.2.4 Synthesis of Pd@Ag Bimetallic Nanoparticles

160 mg of PVP, 25 mg of Ag(acac), 25 mg of $Pd(acac)_2$, and 2 ml of NaI solution (0.15 g/mL) were all added to 10 ml of DMF, respectively. The resulting solution was then transferred to a teflon-lined stainless-steel autoclave. Then, the autoclave was heated at 150 °C for 8 h, cooled down to room temperature and the nano-particles were washed in a 1:8 ethanol/acetone mixture several times at 5000 rpm for 5 min.

2.2.5 Synthesis of Pd@Ag Bimetallic Nano-wires

1 mg of the previously synthesized palladium nanocubes were dispersed in 0.5 ml of nitrogen-saturated water. Then, 1.5 mg of PVP and 1.6 mg of Ag(acac) were added to the mixture and stirred for 2 and 1 min, respectively. The solution was heated in a teflon-lined stainless-steel autoclave for 20 min at 120 °C. The NPs were washed with ethanol, centrifuged at 15000 rpm for 15 min.

For the sample with increased silver content, the same previous protocol was followed, with 1.9 mg PVP, 1.5 mg of Ag(acac), 1 mg of palladium nano-cubes, and 0.8 ml of nitrogen-saturated DI water.

2.2.6 Synthesis of Alloyed Ag-Pd Core-Satellite Nanoparticles

For the synthesis of alloyed AgPd core-satellite nanoparticles, (Ag:Pd= 1:1): 1 ml (0.005 mmol) of silver colloidal NPs solution was washed several times with ethanol, dried with nitrogen flow, and instantaneously dispersed in 0.35 ml of DMF, then transferred to the teflon liner. 2.5 mg of PVP was dissolved in the solution, followed by adding 1.6 mg of $Pd(acac)_2$ and stirred. The resulting solution was sealed and heated in the autoclave for 1 h at 210 °C. Autoclave was cooled down to room temperature and then colloidal solution was stored. Solution was washed several times with ethanol for subsequent characterization. Same protocol was used for the following synthesis except some changes in amount of material.

For the synthesis of (Ag:Pd=1:2) at 210 °C: 4 mg of PVP and 3 mg of $Pd(acac)_2$ were used.

2.2.7 Synthesis of Ag-Pt Bimetallic Nanoparticles

For synthesis of Ag@AgPt nanoparticles, different ratios were attempted. For synthesis of (Ag:Pt= 1:2): 2 ml (0.01 mmol) of silver colloidal NPs solution was washed several times with ethanol, dried with nitrogen flow, and instantaneously dispersed in 0.8 ml of DMF, then transferred to the teflon liner. 12 mg of PVP was dissolved in the solution, followed by adding 4.1 mg of $Pt(acac)_2$, and stirred. The resulting solution was sealed and heated in the autoclave for 1 h at 265 °C. Autoclave was cooled down to room temperature and then colloidal solution was stored. Solution was washed several times with ethanol for subsequent characterization. For ratio variation, same protocol was followed except for some amounts of materials:

For the synthesis of (Ag:Pt=1:3.15), 1.2 ml of DMF, 6.3 mg of $Pt(acac)_2$, and 18 mg of PVP were used.

For the synthesis of (Ag:Pt=1:5.3), 1.8 ml of DMF, 10.6 mg of $Pt(acac)_2$, and 30 mg of PVP were used.

For the synthesis of alloyed (Ag:Pt = 1:4) NPs synthesized at 275°C: 20 mg of PVP, 8 mg of $Pt(acac)_2$, and 1.5 ml of DMF were used.

2.2.8 Synthesis of AgPdPt Trimetallic NPs

2 ml (0.01 mmol) of silver colloidal NPs solution was washed several times with ethanol, dried with nitrogen flow, and instantaneously dispersed in 0.8 ml of DMF, then transferred to the teflon liner. 12 mg of PVP was dissolved in the solution, followed by adding 2.5 mg of $Pt(acac)_2$ and 2.6 mg of $Pd(acac)_2$. The resulting solution was sealed and heated in the autoclave for 1 h at 265 °C. Autoclave was then cooled down to room temperature and then colloidal solution was stored. Solution was washed several times with ethanol for subsequent characterization.

2.3 Characterization Techniques

2.3.1 Transmission Electron Microscopy (TEM)

Transmission Electron Microscopy (TEM) is a powerful technique that has a crucial role in investigating a material's structure at the nanoscale, allowing researchers to gain insights into the morphology and structural characteristics of the material. As its name is given, electrons transmit through the sample, providing a high spatial resolution that enables researchers to analyze features at an atomic level. When equipped with energy dispersive X-ray (EDX) spectroscopy, it allows analysis of the sample's elemental composition, mapping the distribution of different elements within the sample at the nanoscale level. Equipping traditional TEM with scanning transmission electron microscopy (STEM) combines diffraction and imaging at the same time. It relates the compositional with the structural information, enabling an in-depth understanding of the structural, dimensional, and compositional features of the materials analyzed.

For sample preparation: NPs were washed several times with ethanol and then approximately 8 μL was dropped on a carbon coated copper TEM grid. High resolution (HR-TEM) imaging was conducted via the JEOL 2100 JEM HRTEM device at UNAM, Bilkent University. For high angle annular dark field (HAADF-STEM) and EDX analysis, samples were characterized by FEI TALOS F200S TEM 200 kV microscope, at Bayburt University.

For samples imaged at Bayburt University, samples were packaged in a TEM box and took around 3 days for shipping to Bayburt University. On average, imaging of samples took approximately 3-6 days after their preparation. At UNAM, samples were freshly prepared and were imaged on the same day.

2.3.2 X-Ray Diffraction (XRD)

X-ray diffraction is a powerful technique used mainly in materials science-related fields, providing information about the crystallographic structure of many materials. The sample is exposed to X-rays, and the diffraction patterns are studied, revealing information and insight into the material's atomic arrangement. The diffraction pattern is considered a fingerprint for the crystal lattice, providing information about the type of crystal structure and the lattice parameters. Other types of information can be studied and obtained from XRD, including strain and orientation, enlightening researchers on materials' properties and facilitating their interpretation of the physical and chemical behavior.

NPs were washed several times with ethanol and then dropped on a silica wafer, which was cleaned with acetone, ethanol, and DI water, respectively. Samples were characterized with Multi Purpose X-Ray Diffractometer (XRD- MPD) using Cu-Kα radiation ($\lambda = 1.54056$ Å) at UNAM, Bilkent University.

2.3.3 UV-Vis Spectroscopy

Ultraviolet-visible spectroscopy provides insights into the interaction of ultraviolet and visible light with matter. It measures the absorbance or transmittance of the light as it passes through the sample. When light passes through a transparent cuvette-containing solution, the light intensity will be adjusted according to the sample concentration, i.e., a higher concentrated sample solution will absorb more light. Furthermore, the attenuation is proportional to the length of the cuvette. Both factors can be expressed by the absorbance (A) as a function of concentration and cuvette length. According to Lambert-Beer Law:

$$A = \varepsilon \cdot c \cdot l$$

where the absorbance (A) is equal to the product of the extinction coefficient ε, the concentration c and the path length l.

Samples were characterized with UV-Vis-NIR Spectrophotometer Cary - 5000, at UNAM, Bilkent University. All samples were washed with ethanol or ethanol/acetone 1:8 mixture several times, and then a defined concentration of the colloidal solution was dispersed in ethanol. All UV-Vis measurements were taken with ethanol as a dispersant.

Chapter 3

Results and Discussion

3.1 Silver (Ag) Nanoparticles

3.1.1 The Effect of Polyvinylpyrrolidone (PVP)

PVP is known to have multiple roles in the synthesis of nanoparticles. In addition to its role as a capping agent, it can be used as a dispersant and reducing agent [18]. PVP can also control nanoparticle size and shape [19]. In this work, silver nanoparticles were synthesized in the presence of PVP, which facilitated the reduction of Ag(acac) to silver NPs and prevented their aggregation at high temperatures.

Silver acetylacetonate reduction to Ag NPs in the presence of water was reported in literature. However, the thermal reaction at room temperature lasted for 48 hours to complete [20]. Due to the nature of Ag(acac) being insoluble in water, it is difficult for the silver precursor to form a silver complex with water for the reduction reaction to initiate. In my synthesis, adding PVP to water and then Ag(acac) resulted in a homogeneous-black color solution. In the absence of PVP, the solution was inhomogeneous, and I observed silver acetylacetonate powder floating on the water surface. This demonstrates PVP as a suitable dispersant.

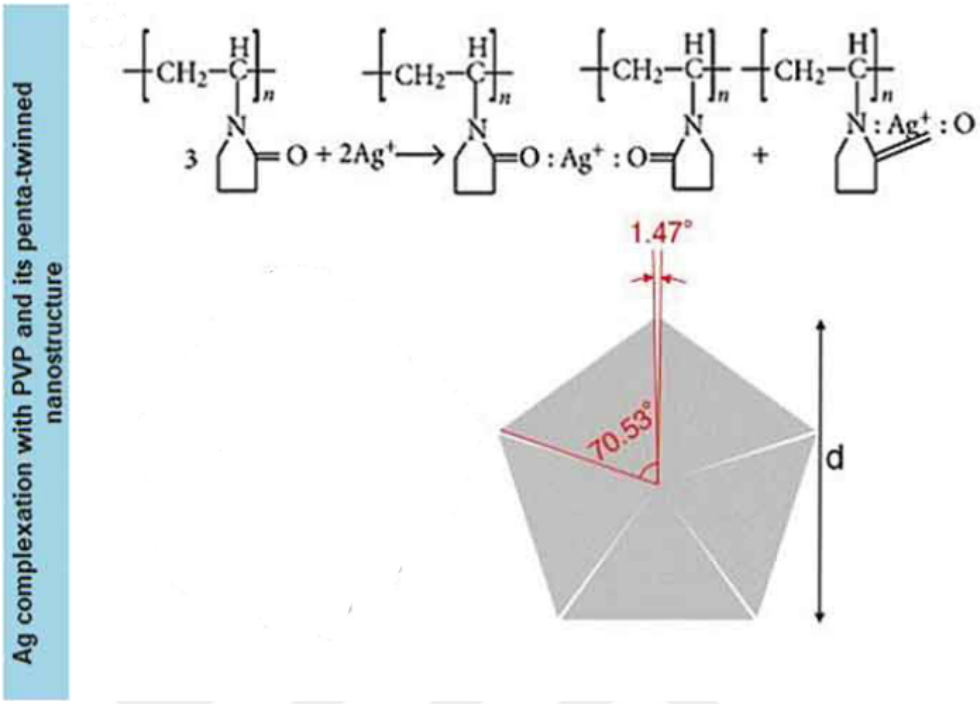

Figure 3.1: Schematic representation of Ag ions complexation with PVP chains. Polar groups (N-C = O) of the PVP chains coordinate with silver ions forming a coordinating complex. The high molecular weight of PVP allows coordination with large silver ions along the long chain (Figure adapted from [24]).

PVP also acted as a capping agent. Proceeding the reaction at a high temperature to shorten the time of Ag(acac) reduction in the presence of nitrogen-saturated water only resulted in chunks of silver NPs formed in my synthesis, where the silver NPs reduced tended to aggregate on the inner wall of the vial due to high temperature. Adding PVP to the solution prevented such a phenomenon from occurring. PVP polyvinyl chains surround silver nanoparticles due to the steric effect that causes anti-agglomeration [21][22]. The nitrogen atom present in the chain is responsible for the protective layer formation and capping of the silver nanoparticles as it coordinates with the silver atom and forms a protective layer [21]. PVP is an amphiphilic and non-ionic polymer, where the vinyl backbone has the hydrophobic part that surrounds the metal particles, and the hydrophilic pendant group interacts with water [23]. This facilitates Ag-water complex formation, where N-C=O coordinates with the silver ions, and the nitrogen also forms hydrogen bonds with water (Fig.3.1).

Fig.3.2 shows the effect of PVP in facilitating the reduction, with color change as an indicator of the reduction. In absence of PVP, silver acetylacetonate powder

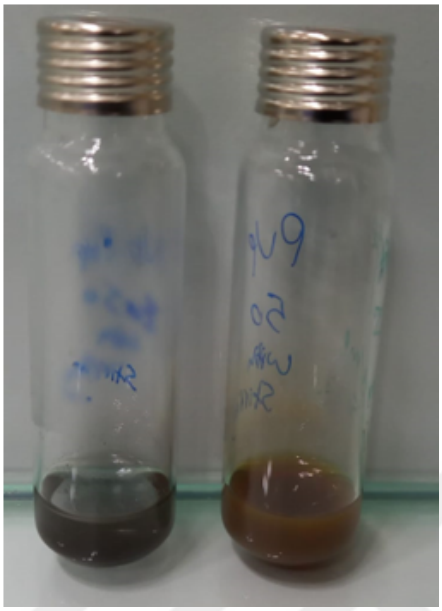

Figure 3.2: Silver NPs synthesized via a dry bath at 50 °C without (left) and with PVP (right).

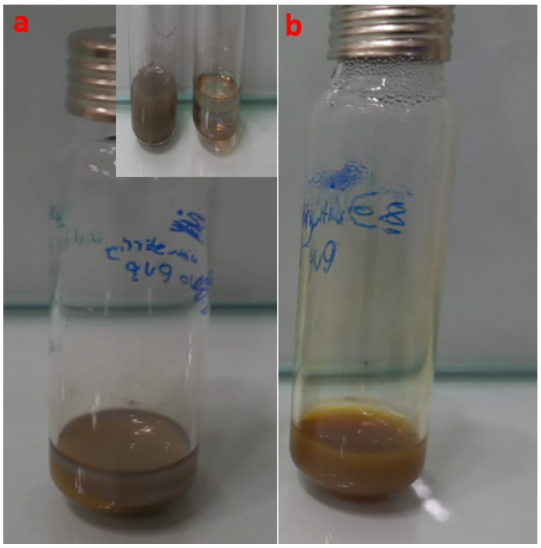

Figure 3.3: Ag NPs synthesized at 80 °C via a dry bath: (a) without adding PVP; inset shows solution after addition of ethanol in an attempt to remove the stuck Ag NPs on the surface of the inner wall of the vial, (b) with addition of PVP.

can be seen floating on the surface of the water, compared to synthesis in presence of PVP.

Temperature was increased from 50 to 80 °C to facilitate reduction without PVP. However, Ag NPs were stuck on the inner wall of the vial, and chunks of Ag NPs were aggregated on the surface of the solution (Fig.3.3a). When attempting to add ethanol and enhance dispersion of NPs in the solution by sonication, the color changes to grey which indicates aggregation of Ag NPs (inset of Fig.3.3a). On the other hand, presence of PVP resulted in a homogeneous colloidal solution, and with a more pronounced color change to brown indicating the synthesis of Ag NPs.

3.1.2 The Effect of Thermal Treatment

The thermal treatment process has a crucial effect on NPs synthesis, where their impact relies on the efficiency of heat transfer during the synthesis, resulting in a stark difference in, size distribution and shape of the nanoparticles synthesized. Enhancing heat transfer for thermal reactions allows control of several parameters. Dry and water bath thermal processes were attempted to study their effect on the size distribution of Ag NPs. A dry bath experiment was held in an oven at a specified temperature, and a water bath experiment was held using a beaker filled with water and heated on a hot plate, with an aluminum foil covering it. A thermometer was used to measure the temperature.

First, a dry bath was attempted at 50°C, 80 °C, and 130 °C. The thermal reaction proceeded for 20 min for all three samples, and color variation was apparent as lower temperature synthesis at 50 °C showed dark brown, while the highest temperature of 130 °C yielded light brown (Fig.3.4). In the water bath medium, the color of the solution turned light brown after 2.5 min, indicating the most efficient heat transfer.

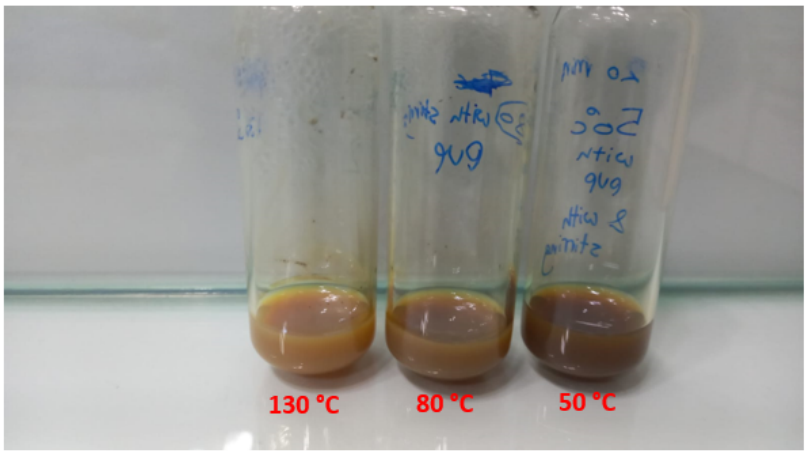

Figure 3.4: Ag NPs reduced at temperatures 50, 80, and 130 °C, respectively, from right to left. Color becomes lighter demonstrating the more reduction of silver.

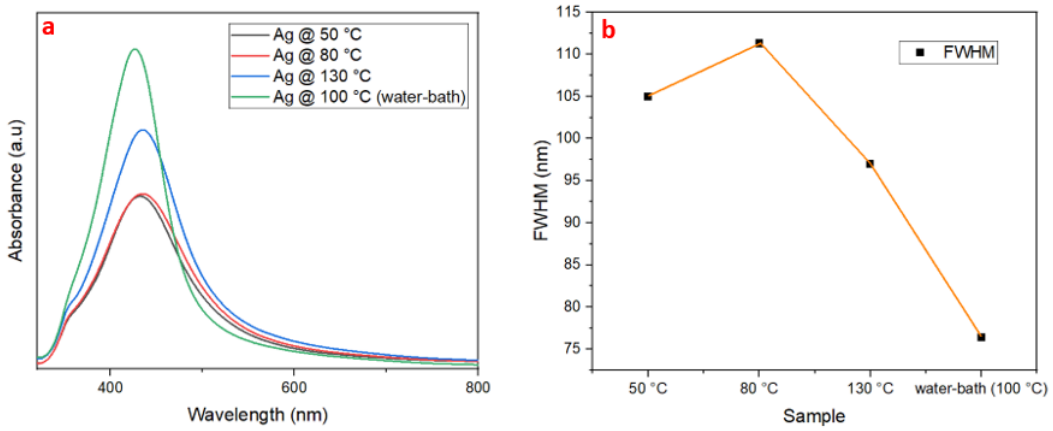

Figure 3.5: (a) UV-Vis spectra of Ag NPs synthesized via dry and water bath thermal processes at varied temperatures, (b) FWHM showing the size distribution of synthesized Ag NPs.

Uv-Vis was used to monitor and track the complete reduction of the silver metal precursor. The UV-Vis spectra are shown for the Ag NPs synthesized under different temperatures and methods of thermal treatment (Fig.3.5a). The enhanced LSPR in the figure indicates the formation of more silver NPs where their synthesis are close to complete [25]. The dry bath samples synthesized at 50, 80, and 130 °C temperatures showed LSPR peaks at 432, 435, and 435 nm, respectively, which are very close to each other. The water-bath medium showed a peak at 426 nm. The formation of the pronounced peaks around 426, 432, and 435 nm indicates the formation of silver nanoparticles [26]. The sample heated in the water bath showed the best results, compared to dry bath experiments, where the LSPR peak was more pronounced, with the highest absorbance. This indicates the enhanced heat transfer in case of the water-bath medium, where more silver NPs were formed. The isosbestic peaks at 355 nm demonstrate the release of the Hacac ligand [20], where firm peaks are shown for the dry bath experiments and a diminished peak in the water bath medium indicating the efficient release of protonated ligand and formation of silver NPs in the water bath experiment.

The LSPR peak position and FWHM also give an idea about the sample's average size and size distribution, respectively. In dry bath experiments, the

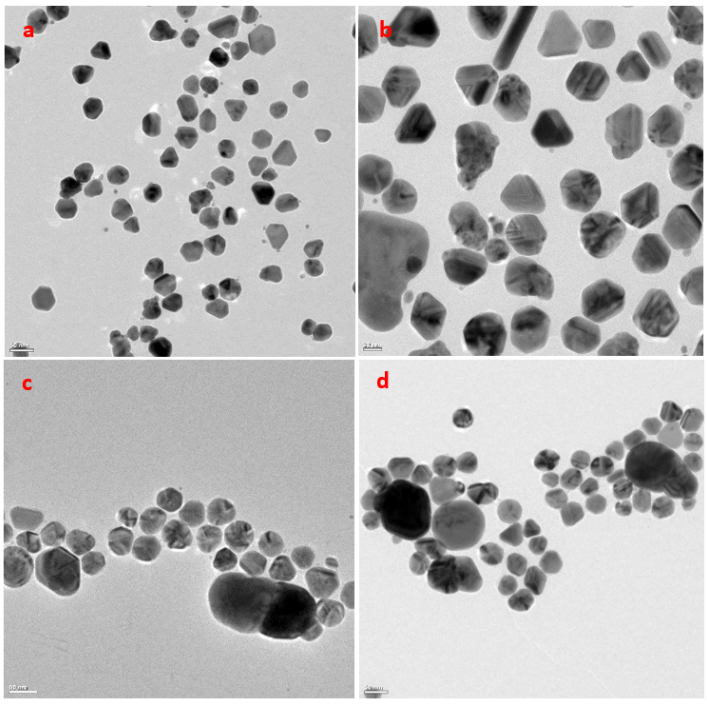

Figure 3.6: (a and b): Ag NPs formed at 50 °C, (c and d): Ag NPs formed at 130 °C by the dry bath method. Scale bars are 50, 20, 50, and 50 nm for a-d, respectively.

peak of 80 °C and 130 °C is red shifted compared to 50 °C. This would be due to the larger size of some nanoparticles, as the average sizes of Ag NPs synthesized at 50 and 130 °C were 45 ± 5.4 and 49.3 ± 4.6 nm, respectively, excluding large NPs with sizes above 55 nm. As the nanoparticles are getting more formed and at a low temperature, sizes of nanoparticles are randomly distributed and tend to have relatively larger nanoparticles' size unevenly grown due to the insufficient temperature for getting a well-distributed size. The FWHM for the 80 °C sample gave the highest value, indicating the broadest size distribution, where at 130 °C the FWHM was the lowest among those dry bath synthesized samples. At 50 °C, silver nanoparticles did not have enough temperature to reduce Ag(acac) in the fixed time amount of 20 minutes. Subsequently, the UV-Vis spectrum slightly blue shifts compared to the 80 and 130 °C. It is supposed that larger particles form at lower temperatures, but maybe due to insufficient time, particles only grew to an extent, with a FWHM of 104.5 nm. In 80 and 130 °C, chunks of larger silver nanoparticles should be formed, contributing to the 435 nm peak, which

can be seen in TEM images in Fig.3.6. Due to inefficient heat transfer in dry bath experiments, NPs were randomly distributed with a myriad of sizes and shapes for all three samples [27][28].

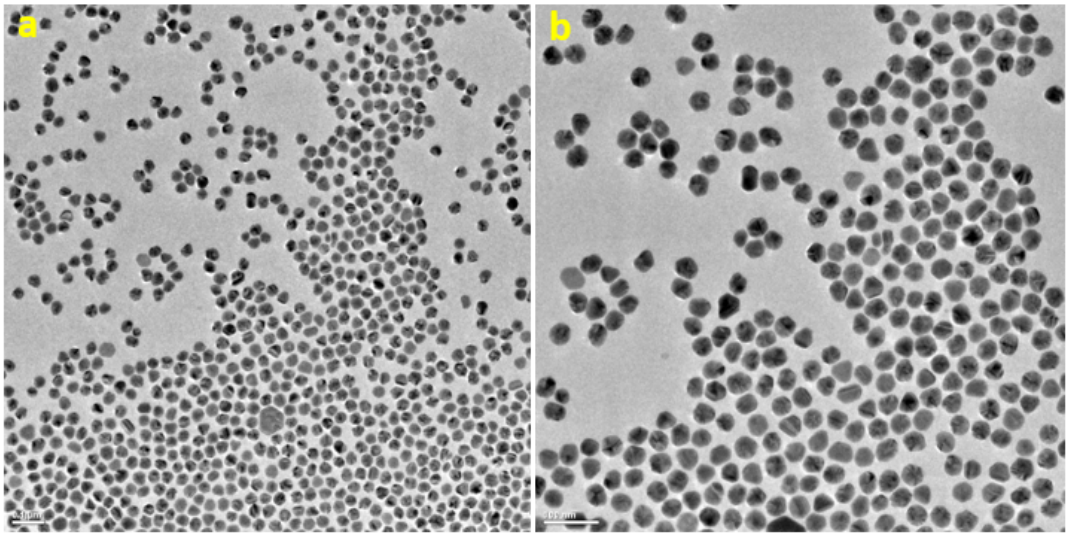

Figure 3.7: TEM images of Ag NPs synthesized via water-bath medium at 100 °C, scale bars are 0.1 µm and 0.1 nm for (a) and (b), respectively.

In the water bath experiment, a blue-shift in the peak of silver to 426 nm indicated smaller size of NPs. The FWHM also shows the size distribution to be the lowest among all samples, which indicates the uniform size of nanoparticles (Fig.3.7).

As can be seen from Fig.3.8, nanoparticles have a close size distribution. Using imageJ software, the particles size distribution was calculated to give 34.6 ± 5.5 nm.

In the absence of any other impurities, PVP binds strongly to 100 silver facets [29][30], where it directs some of the silver seeds to grow in the ⟨111⟩ directions and have defects, forming folded twinned nanoparticles [31][32] and other multi-faceted NPs (Fig.3.9).

Fig.3.10 shows the XRD pattern for silver nanoparticles synthesized by water-bath experiment. The face centered cubic (fcc) structure was identified with peaks

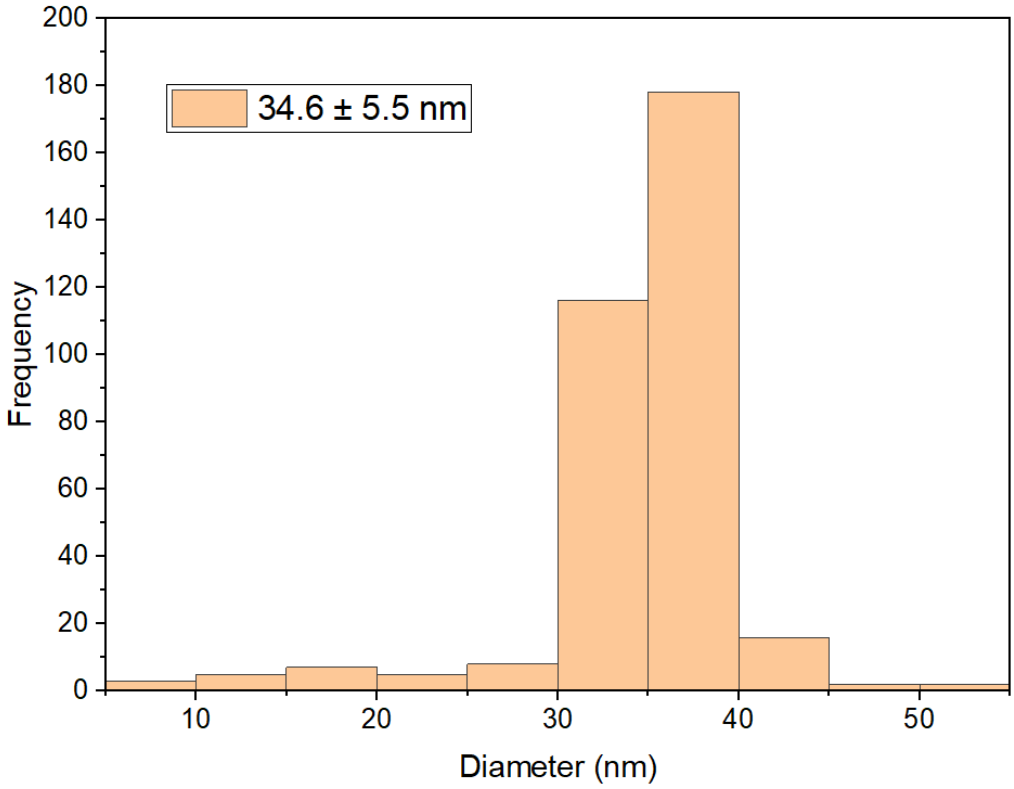

Figure 3.8: Histogram showing size distribution of Ag NPs synthesized in water-bath medium at 100 °C

at 38.20, 44.40, 64.60, 77.60 and 81.75°. In accordance with crystallographic lattice planes, the respective planes for each peak correspond to (111), (002), (022), (113), and (222) (Ref: Joint Committee on Powder Diffraction Standards, JCPDS file No. 04-0783). The highest intensity corresponds to the (111) plane which is typical for the fcc crystal structure.

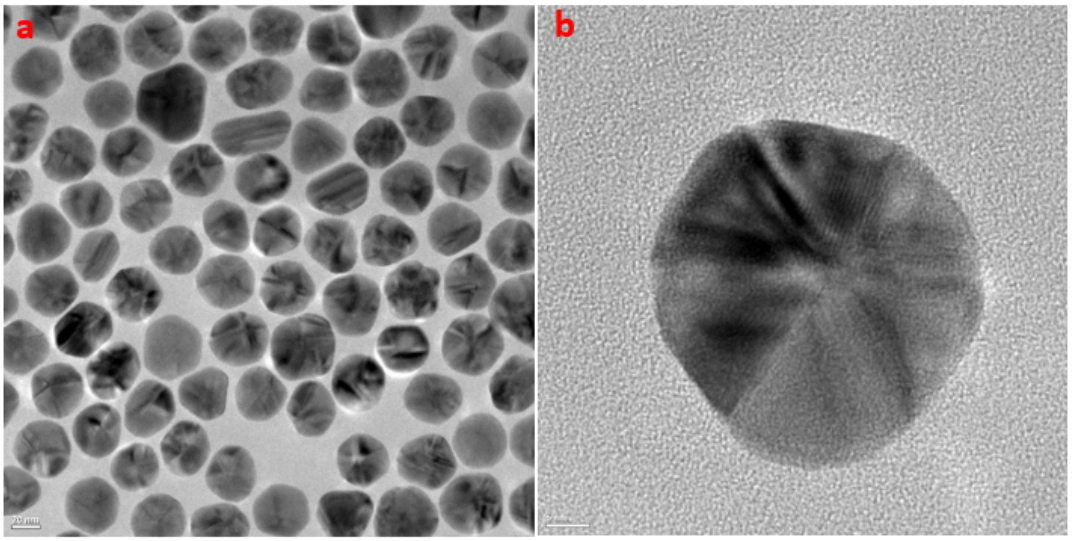

Figure 3.9: TEM images for Ag NPs synthesized by the water-bath experiment at 100 C°, with scale bars of 20 and 5 nm for (a) and (b), respectively.

Scherrer's equation was used to estimate the size of silver NPs. The Scherrer equation is given by:

$$D = \frac{K\lambda}{\beta \cos(\theta)} \tag{3.1}$$

Where:

D is the average crystallite size

K is the Scherrer constant (typically around 0.9)

λ is the wavelength of the X-ray or neutron radiation

β is the Full Width at Half Maximum (FWHM) of the diffraction peak

θ is the Bragg angle

Scherrer's equation gave an average size of 30.1 nm, which is close to 34.6 $\pm$ 5.5 nm, measured from TEM images.

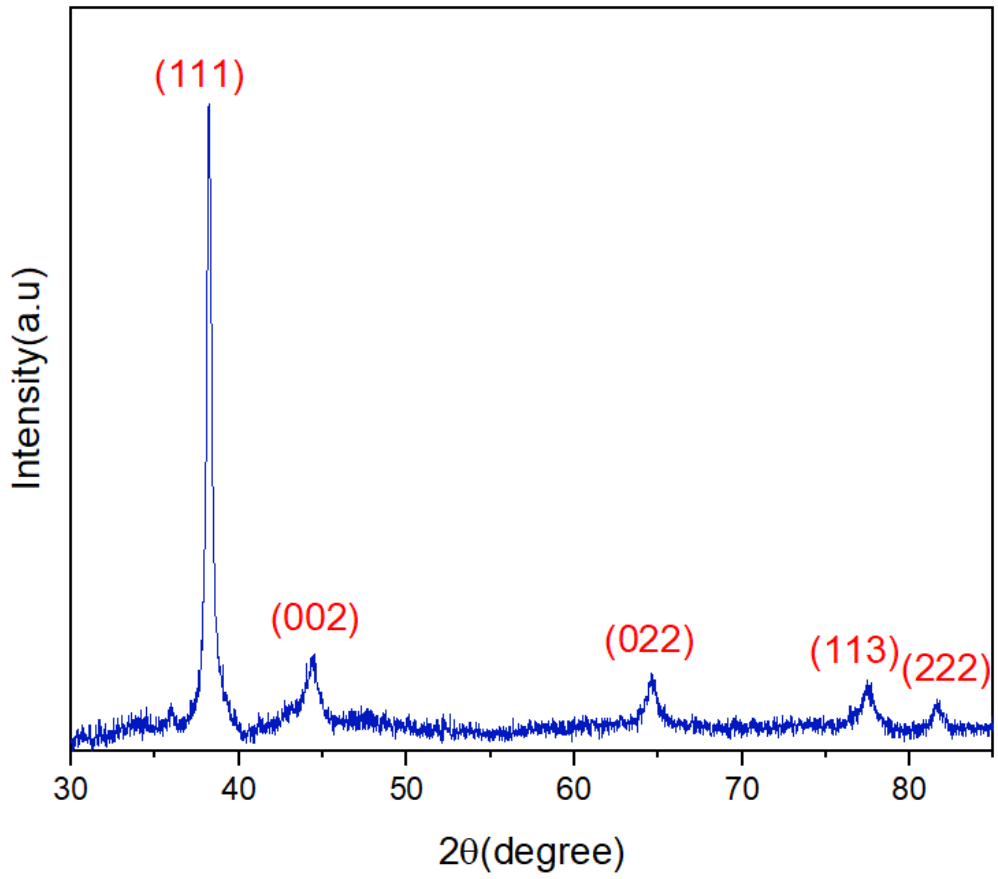

Figure 3.10: X-ray diffraction of Ag NPs synthesized by the water bath experiment at 100 °C

3.1.3 Stability of Synthesized Ag Nanoparticles

Silver NPs' stability was tested for a period of one month. NPs were stored at 2–8 °C in the same mother-stock solution. The color of the solution was tracked for a month. No change in the LSPR peak or the color was detected. However, when when a drop of the NP solution was dried on a TEM grid and shipped for TEM imaging, some samples exhibited core-satellite structure, as shown in Fig.3.11a-c. This behavior was predicted to be due to heat effect. Exposing silver nanoparticles to room temperatures or higher resulted in the instability of silver nanoparticles, where their size and shape changed [33]. Clusters of silver, perfectly spherical, separated from silver cores to their surface, forming satellites. The spherical shape was formed to reduce the surface energy, where the sphere

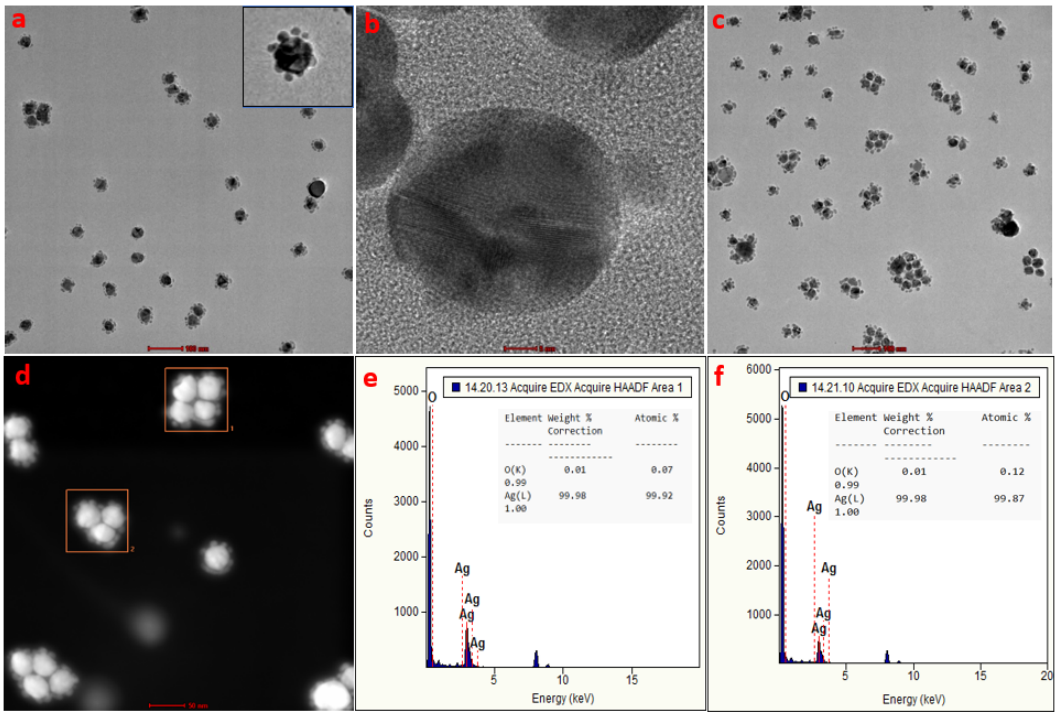

Figure 3.11: HAADF-TEM-EDX analyses for Ag monometallic NPs after being dropped on a TEM grid and aged for 3 days: (a-c) TEM images of silver nanoparticles with inset in (a) showing Ag core-satellite morphology, (d-f) shows dark-field TEM image with EDX mapping of corresponding areas. Scale bars are equivalent to 100, 5, 50, and 50 nm, from (a-d), respectively.

has the lowest energy of all other shapes. It can be seen that most of the NPs themselves are not coalescing with each other, probably due to the steric effect of PVP. PVP caps the main NPs while the satellites formed are not capped by PVP, and so they tend to form small aggregates with other satellites.

EDX analysis was performed to ensure that the formed Ag satellites are not a result of oxidation of silver in the presence of air, as NPs were imaged after approximately five days after the sample preparation. EDX analysis showed that the core-satellite structures are only silver monometallic NPs, with negligible amount of oxygen present (Fig.3.11e-f).

However, the same phenomenon was observed when attempting to coat silver NPs with palladium, where a core-satellite structure has formed. In order to

confirm if a spontaneous thermal reaction is the reason for satellite formation, silver NPs were post-treated in the same environmental conditions of synthesizing Ag-Pd alloyed core-satellite NPs. Synthesized silver NPs were washed several times with ethanol, dried with a flow of nitrogen gas, and then dispersed in DMF. PVP was added, and the solution was sealed in an autoclave and held at 210 °C for an h. After the reaction, the solution turned dark green. UV-Vis and TEM were measured to study the changes in the sample.

UV-Vis spectroscopy determined the difference between Ag NPs and post-treated ones. Post-treated silver NPs show two low-intensity broad peaks at 430 and 617 nm (Fig.3.12). This shows that they were significantly affected when exposed to the same temperature used to reduce palladium on silver core NPs. TEM images show that silver NPs broke down to smaller NPs where they could not withstand elevated temperatures (Fig.3.13a-b). Ag NPs underwent ripening, where their size and shape completely deteriorated. This demonstrates the instability of Ag NPs under elevated temperatures when post-treated. Further studies need to be carried out for this phenomenon. Nevertheless, both previous phenomena may explain the satellite formation in the Ag-Pd alloyed core-satellite structure.

As Ag NPs were stable in the mother-stock solution, another experiment for the synthesis of Ag NPs was attempted by synthesizing Ag NPs at 210 °C in an autoclave in the presence of only water and PVP. After the reaction, the color was light brown. Surprisingly, Ag NPs showed high stability at high temperatures (3.13c-d). UV-Vis spectrum shows the LSPR peak at 417 nm, which points to a lower average size of NPs with a pronounced LSPR peak. The average mean size of NPs was calculated to be 31.9 $\pm$ 4.4 nm, less than that of 34.6 $\pm$ 5.5 nm, obtained from the water bath at 100 °C.

It can be concluded that when silver NPs are not in their mother-stock solution, they tend to undergo spontaneous thermal reaction at room temperature. However, further studies are needed to confirm this phenomenon.

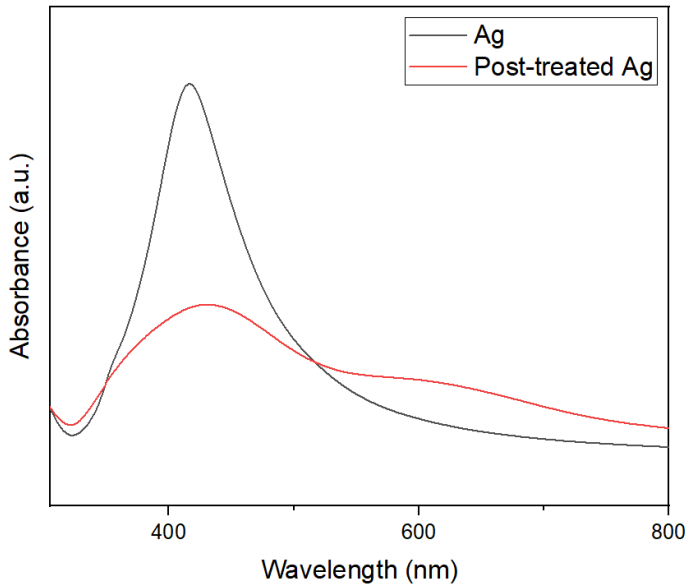

Figure 3.12: UV-Vis spectra of post-treatment of synthesized Ag NPs at 210 °C for 1 h and Ag NPs synthesis at 210 °C for 1 h

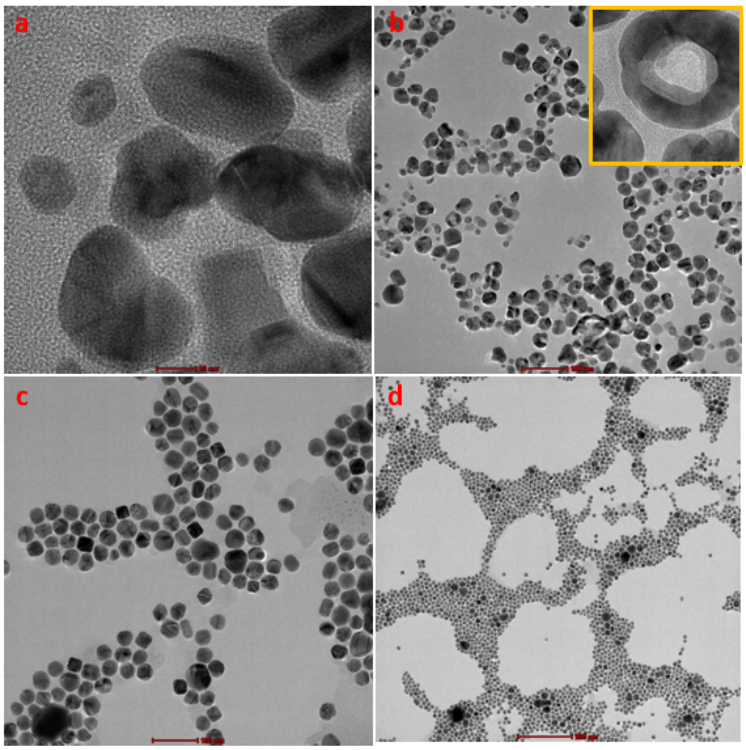

Figure 3.13: TEM images for (a-b) Ag NPs post-treated and (c-d) Ag NPs synthesized at 210 °C

3.2 Palladium (Pd)

3.2.1 Palladium Nano-Cubes

Palladium nano-cubes were synthesized according to a reported method to form nano-cubes [11]. PVP played a role as a capping agent in the synthesis, and sodium iodide played a significant role in forming the nano-cubic shape for the nanoparticles, acting as a shape regulator. Multiply twinned palladium nanoparticles were formed when sodium iodide wasn't used [11]. Palladium nano-cubes were synthesized as a core for reducing silver and forming bimetallic Pd@Ag nanoparticles. It has been reported that different halides were used to form nano-cubes. However, none gave the same result as the sodium iodide when using the DMF as a reducing agent and replacing the NaI with other halides of Cl^- and Br^-, and F^-; no nanocube formation was observed. Instead, multiply twinned NPs formed, demonstrating the significant role of the iodide ions in the synthesis when using $Pd(acac)_2$ as the metal precursor[11]. The choice of the reducing agent is critical as the reaction is temperature dependent, i.e., when increasing the temperature, more reduction of the metal precursor is observed [34]. Fig.3.15 shows Pd nano-cubes synthesized using sodium iodide and DMF. When using sodium bromide with ethylene glycol as a reducing agent, it was observed that palladium nanocubes were also formed in a monodisperse manner [11].

TEM was used for analyzing the size and crystalline nature of Pd nano-cubes. The lattice spacing for the palladium nano-cubes was calculated to be 0.194 nm, which corresponds to the (200) plane. An average size of the Pd nano-cubes was measured as 11.6 nm, as shown in Fig.3.14 and Fig.3.15b.

Sample was characterized using XRD for crystallinity of the synthesized Pd nano-cubes (Fig.3.15c). The peaks shown in the XRD pattern are assigned to 40.11, 46.66, 68.12, 82.10, and 86.62°, corresponding to fcc palladium (111), (002), (022),(113), and (222) planes. (ref: JCPDS No. 98-064-8674). EDX analysis was also performed to ensure the presence of pure palladium NPs.

Zeta potential of the synthesized Pd nanocubes were measured. Three independent measurements showed the zeta potential values around -20 mV, which indicates negative charges were formed around the Pd nanocubes (Fig.3.15e). Zeta potential is often used as an indicator of the nanoparticle stability. As nanoparticles with a zeta potential value greater than ±30 mV is generally considered stable [35], the synthesized Pd nanocubes show incipient instability.

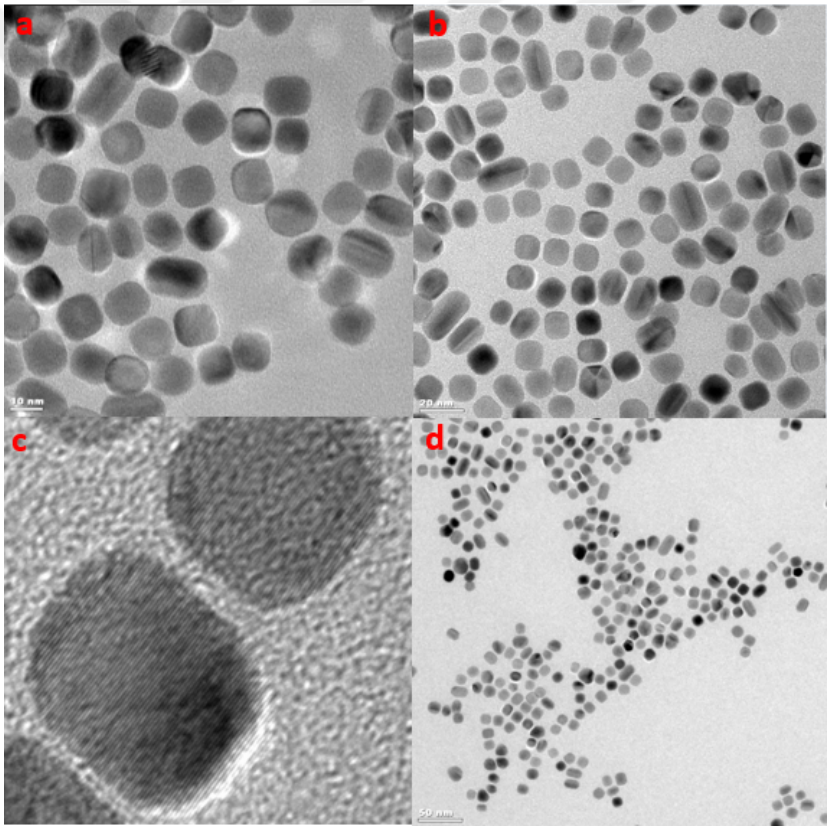

Figure 3.14: TEM images of Pd nanocubes at different magnifications. Scale bars are 10, 20, 5, and 50 nm for (a-d), respectively.

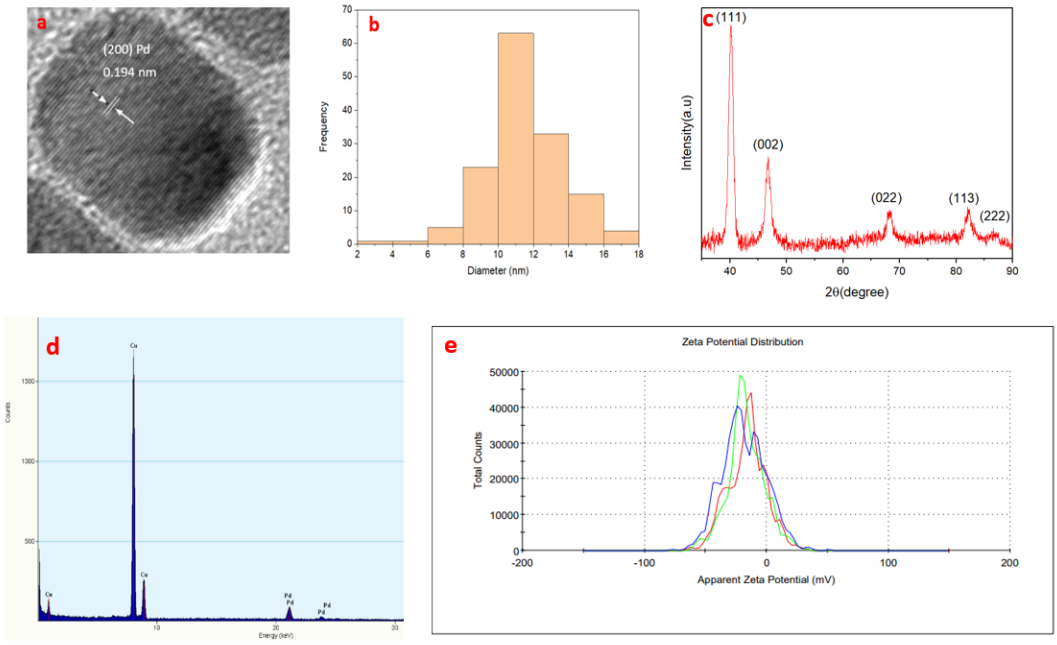

Figure 3.15: Characterization of Pd nanocubes: (a) HR-TEM image showing d-spacing of lattice, (b) shows size distribution of nano-cubes, (c) X-ray diffraction (XRD) analysis showing fcc crystal structure of the as-synthesized pd nanocubes with the corresponding planes, (d) EDX analysis mapping, and (e) zeta potential measurement repeated three times for precision, which gave an average of -20 mV.

3.2.2 Palladium Nanoparticles

In a two-pot synthesis method, silver metal precursor was added to the palladium nanocube seeds for the reaction. The same protocol and conditions of the palladium nanocube synthesis were followed, except for adding Ag(acac) and starting with already synthesized palladium seeds. TEM images were taken, and Pd nanoparticles also showed a perfect spherical shape. No presence of silver was detected, as shown in the EDX (Fig.3.16d).

It is proposed that silver precursor was not reduced in the reaction because DMF acted as a very poor reducing agent for Ag(acac). When trying to use the same synthesis protocol of palladium nanocubes for the synthesis of silver nanoparticles in DMF as a reducing agent and Ag(acac) as a metal precursor, only a tiny amount of silver was formed as the color was light yellow, which does

not match with the amount of silver metal precursor used, which was 25 mg.

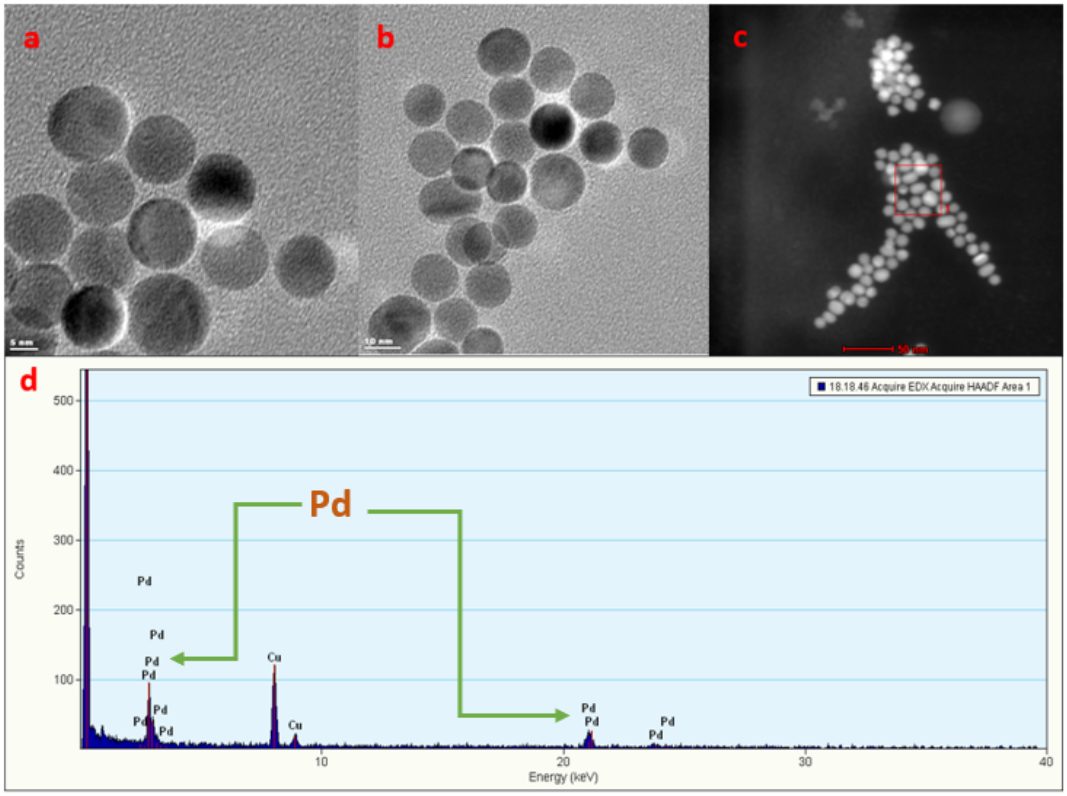

Figure 3.16: Two pot-synthesis where palladium nanocubes seeds were already prepared before the reaction: (a-b) bright-field TEM images for Pd NPs, (c) dark-field image and (d) EDX mapping for the selected area in (c).

For reduction of Ag(acac), the silver complex with water and PVP is first formed. Then, the ligand of Hacac is released in addition to hydrogen peroxide, which was mentioned in the literature as an oxidative etchant for silver [36][37][38]. Silver, during decomposition and formation of hydrogen peroxide, it might also result in partial decomposition of hydrogen peroxide. On the other hand, palladium nanocatalysts are used for producing hydrogen peroxide [39]. Herein, palladium nano-cubes (200) facets were etched forming perfect spherical NPs. Perfectly spherical nanocrystals show different optical properties from faceted nanoparticles [40][41], especially when nanoparticles form dimers to generate surface plasmon coupling [42]. It is expected that our two-pot synthesis method that uses Ag(acac) to etch the surface of Pd nanocubes, has a potential to make such perfectly spherical nanoparticles and therefore needs further study.

3.3 Pd@Ag Bimetallic Nanostructures

3.3.1 Pd@Ag Nanoparticles

Pd nano-cubes were used as a core for later formation of silver on Pd seeds. Ag(acac) reduced in water and PVP. Pd@Ag NPs were synthesized in a one-pot synthesis, where palladium and silver acetylacetonates were placed in the autoclave for 8 hours at 150 °C, and then the nanoparticles were washed with a mixture of ethanol and acetone; details are shown in the experimental section. TEM images were taken for bimetallic nanoparticles, as shown in Fig.3.17. Silver was present in EDX analysis in small amount, which indicates the formation of bimetallic nanoparticles (Fig3.17a).

Reduction of silver metal precursor is possibly due to the NaI that was added as an aqueous solution to the reaction, where PVP was also present. As mentioned in a previous section, PVP facilitated the reaction, and the small amount of water got oxidized to hydrogen peroxide. Subsequently, the silver metal precursor was only slightly reduced due to the small amount of water present in the reaction, forming bimetallic NPs.

It could also be observed that in the one-pot step synthesis, the NPs were not perfect spheres, when compared to the two-pot synthesis. When silver and palladium precursors were reduced simultaneously, the NPs were not perfect spheres as of the competition between the iodide ions and probably, hydrogen peroxide, in formation of the spherical nanoparticles. The iodide ions- as previously mentioned- are shape regulators and give the cubic shape for the palladium nanoparticles in the DMF system. Silver acetylacetonate ligand-on the other hand- coordinates with water and reduces the metal center, resulting in the oxidation of water to hydrogen peroxide, acting as an oxidative etchant resulting in faceted Pd@Ag bimetallic NPs. However, further experiments need to be held to ensure the reason behind etching the edges of Pd nano-cubes.

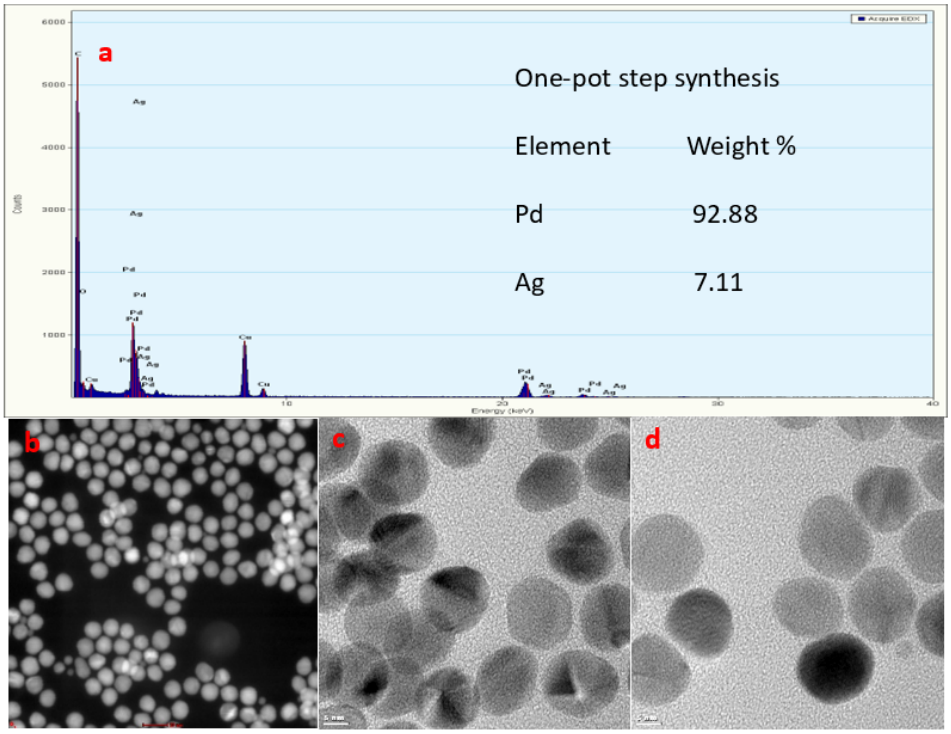

Figure 3.17: EDX and TEM images for a one-pot synthesis of Pd@Ag bimetallic NPs: (a) EDX mapping, (b) dark and (c-d) bright-field TEM images. Scale bars are 20, 5, and 5 nm for (b-d), respectively.

3.3.2 Pd@Ag Nanowires

Pd@Ag bimetallic nanowires were synthesized with a suitable amount of water and PVP as a capping agent. Fig.3.18 shows the formation of Pd@Ag bimetallic nanowires. Pd nanocubes were truncated to become spheres, and silver-connected palladium nanoparticles formed nanowires. These nanowires can be used in different applications, such as sensing [43]. Through line scan analysis, it can be shown that the nanoparticles are either entirely covered with silver forming a full core-shell structure, or form a low class core-shell structure, where silver connects palladium NPs partially.

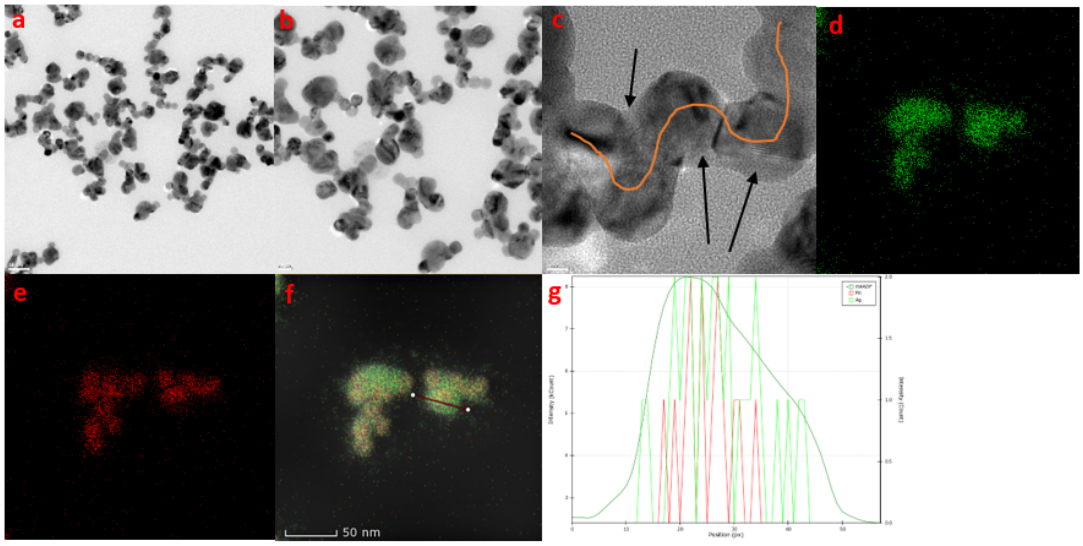

Figure 3.18: (a-c) TEM images showing the morphology of Pd@Ag bimetallic nanowires; where black arrows in (c) show silver connecting Pd NPs and orange line demonstrates the linkage of Pd NPs by silver forming nanowires, (d-f) HAADF-STEM mapping for (d) Ag, (e) Pd, (f) integration Ag and Pd showing area where line scan profile is analyzed and (g) line scan profile showing the distribution of silver (green) with palladium (red). Scale bars are 50, 20, and 5 nm, for (a-c), respectively.

X-ray diffraction was also used to analyze Pd@Ag bimetallic nanowires, and study their crystallinity (Fig.3.19). Silver peaks correspond to 38.20, 44.40, 64.60, 77.60, and 81.75°. Palladium peaks correspond to 40.11, 46.66, 68.12, 82.10, and 86.62°. A peak is detected at 36°, which could refer to an organic byproduct from silver interaction with PVP, as it was observed when mono-metallic silver was synthesized in the previously explicated section of silver. From the XRD spectrum, it can be seen that the intensity of the peak location of (111) facets for palladium is higher than that of silver. Palladium acted as a disturbance for the formation of highly intense (111) silver planes, allowing silver to get reduced and connect palladium nano-cubes that were truncated to spherical NPs.

UV-Vis analysis was performed to confirm the formation of bimetallic NPs. Palladium is known as a catalytic metal, which shows broad absorption in the UV range [44], and the addition of silver gives rise to LSPR in the visible range, which is significant in photocatalytic applications. A peak at 408 nm showed the

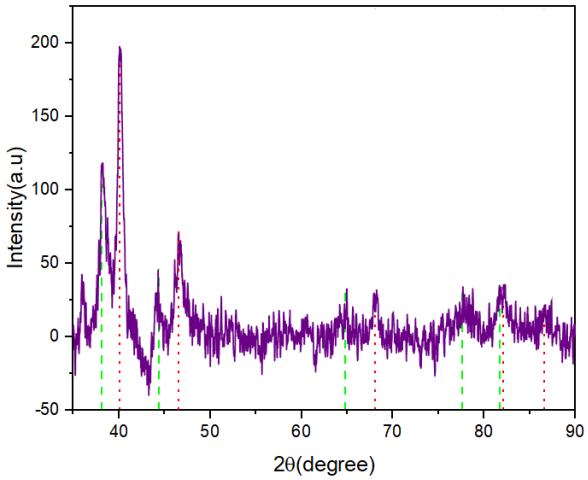

Figure 3.19: X-ray diffraction (XRD) spectrum for Pd@Ag nanowires, green dashes refer to silver peaks and red dots refer to palladium peaks.

presence of silver in the Pd@Ag nanowires, as shown in Fig.3.20.

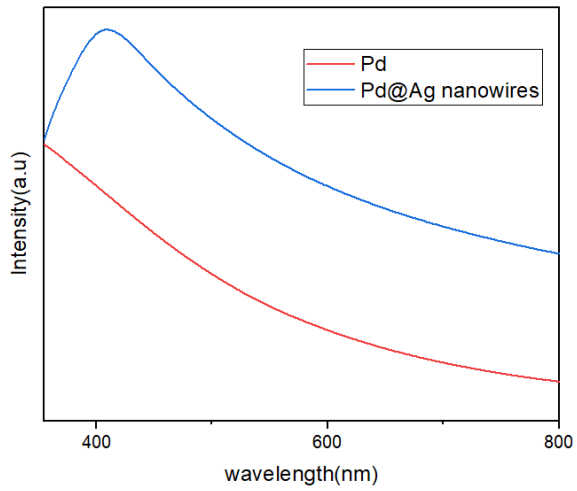

Figure 3.20: UV-Vis spectra for bare Pd nano-cubes (red) and Pd@Ag nanowires (blue).

3.4 Ag-Pd Alloyed Core-Satellite Nanoparticles

Silver monometallic nanoparticles were used as the core for the subsequent reduction of palladium to form the bimetallic alloyed core-satellite NPs. Palladium was reduced by using DMF as a reducing agent and $Pd(acac)_2$ as a metal precursor in the presence of PVP as a capping agent. The resulting nanoparticles formed core-satellite nanoparticles due to the effect of silver instability when post-treated at high temperatures (Section 3.1.3). The reaction was attempted at 210, and 265 °C to form Ag-Pd alloyed core-satellite NPs. We chose these three temperatures to control the formation of the core-satellite structure. The change in temperature would modulate the rate of satellite formation from the silver core NPs relative to the rate of reduction of palladium.

3.4.1 Ag-Pd alloyed core-satellite NPs @ 210 °C

A high temperature was attempted to form AgPd and AgPd alloyed core-satellite NPs at different palladium concentrations. The color of the solution changes to dark brown (Ag:Pd=1:1) and turns black at higher Pd concentrations (Ag:Pd=1:2). The mean size of the core nanoparticles was measured to be around 41.6 ± 4.1 nm, compared to mono-metallic silver counterparts, where average size was measured to be 34.6 ± 5.5 nm. Due to the elevated temperature and the defects formed from the replacement reaction, a rapid inter-diffusion of palladium atoms into the silver core in a multi step process formed alloyed NPs [57]. The synthesis conditions suppressed the formation of any hollow structures.

The synthesized alloy NPs were examined using UV-Vis spectroscopy. In Fig.3.21a, the silver peak at 426 nm is blue-shifted to 410 nm in the case of the AgPd core-satellite NPs at a Ag:Pd ratio of 1:1, confirming the evolution of bimetallic NPs [45]. Increasing the palladium ratio to double resulted in the entire dampness of the silver LSPR peak.

To further study the nature of formed NPs, XRD spectra was analyzed for both

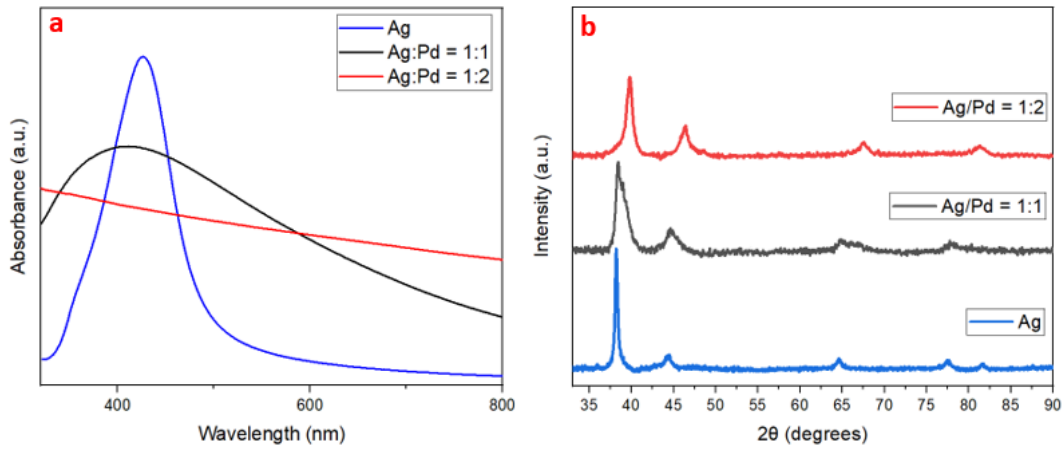

Figure 3.21: (a) UV-Vis spectra for the Ag-Pd alloyed core-satellite NPs synthesized at 210 °C and (b) X-ray diffraction pattern for Ag and Ag-Pd alloyed core-satellite.

samples and compared with silver mono-metallic NPs(Fig.3.21b). The AgPd (1:1) NPs showed the peaks at 38.44 (with a small peak forming at 38.95), 44.63, 64.66, and 77.83°. Compared to the peaks of the bare Ag NPs, the peaks from the AgPd (1:1) were shifted and broadened, confirming the formation of the alloyed NPs. A crystal lattice calculated to be 4.065 Å compared to 4.094 Å of Ag, with a lattice distance changed from Ag (111) of 0.235 nm to 0.234 nm. The peak at 64.66° showed more dramatic changes such as broadening and additional peak formation at 65.30°. The peak at 77.83° was also broadened, while the silver peak at 81.75° disappeared in the case of AgPd NPs. Increasing the palladium concentration resulted in a complete shift in the XRD peaks corresponding to 39.76, 46.37, 67.45, and 81.63°, shifting towards palladium peaks forming a complete alloy, with a lattice distance changed from 0.235 nm to 0.226 nm, which shows the alloyed AgPd (111) [46].

Fig.3.22 shows TEM imaged for Ag-Pd alloyed core-satellite structure, which suggests the formation of satellites before the reduction of palladium. This indicates that choosing the right temperature is essential for the silver core to form satellite particles. This can conclude that selecting the right temperature is essential for the silver decomposition rate to satellites, where it should react with

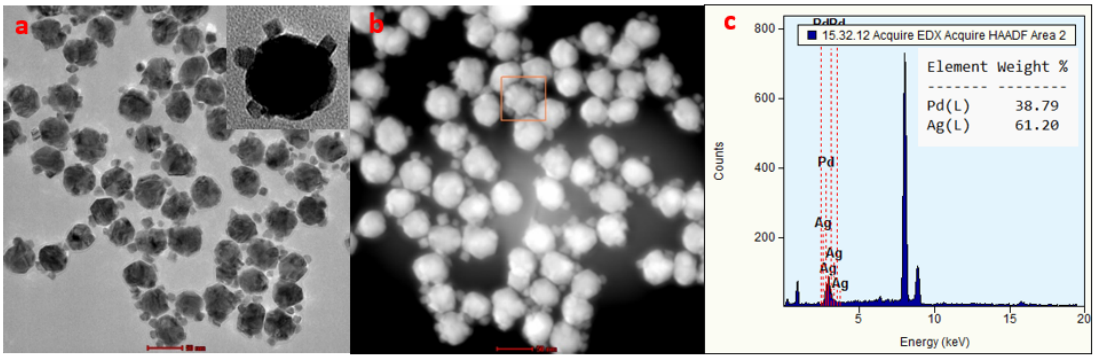

Figure 3.22: TEM-EDX analysis for (Ag:Pd= 1:1.6) synthesized at 210 °C;(a) bright-field TEM image of AgPd core satellites with the inset showing the morphology of the core-satellite, (b) dark-field image and (c) EDX mapping for the corresponding core-satellite particle indicated in the square in (b).

palladium before getting detached.

PVP is expected to control the shape of nanoparticles [46][47]. Herein, Pd gets reduced on the silver spherical satellites, satellite particles forming different random shapes, including cubic and concave nano-cubes (Fig.3.22 an inset). A set of syntheses with varied concentrations of PVP may reveal more homogeneous and defined shapes of satellites. EDX analysis shows the metal content in the core-satellite nanoparticles in Fig.3.22c, which naturally has a higher silver content due to its larger size.

Further study on the elemental distribution was examined using the HAADF-STEM mapping technique. Fig.3.23d shows the presence of palladium and silver in the sample, confirming alloy formation with core Ag and satellite. The line-scan profile further confirms this result, where palladium formed an alloy all over the silver NPs.

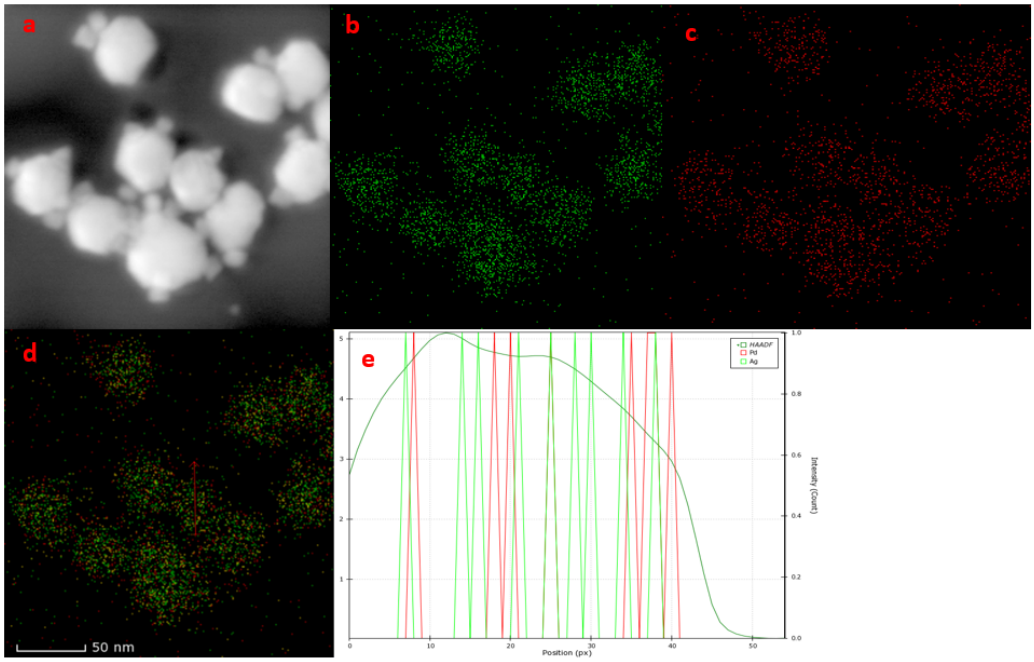

Figure 3.23: HAADF-STEM images for (Ag:Pd= 1:1.6) synthesized at 210° C: (a) dark-field TEM image, (b-d) STEM image of silver, palladium, and the corresponding EDX mapping showing core-satellite nanoalloys, (e) line scan profile along the line path (red arrow) of the particle in (d). Scale bar is 50 nm for (a-d).

3.4.2 Ag-Pd Alloyed Core-Satellite NPs @ 265 °C

Increasing the reaction temperature to 265 °C resulted in fused nanoparticles. Increasing the temperature facilitated silver NPs to degrade into small NPs uncontrollably. The rate of silver degradation was higher than that of palladium reduction, resulting in an increased number of satellites detached from the silver core and NPs fused, forming aggregated nanostructures (Fig.3.24). UV-Vis analysis shows a broad peak, which suggests the decomposition of silver into several sizes due to exposure to high temperatures. XRD analysis shows separated peaks, representing Ag and AgPd (with higher Pd content) with 0.226 nm lattice distance corresponding to AgPd (111). AgPd peaks corresponded to 39.67, 46.29, 67.94, and 80.92°.

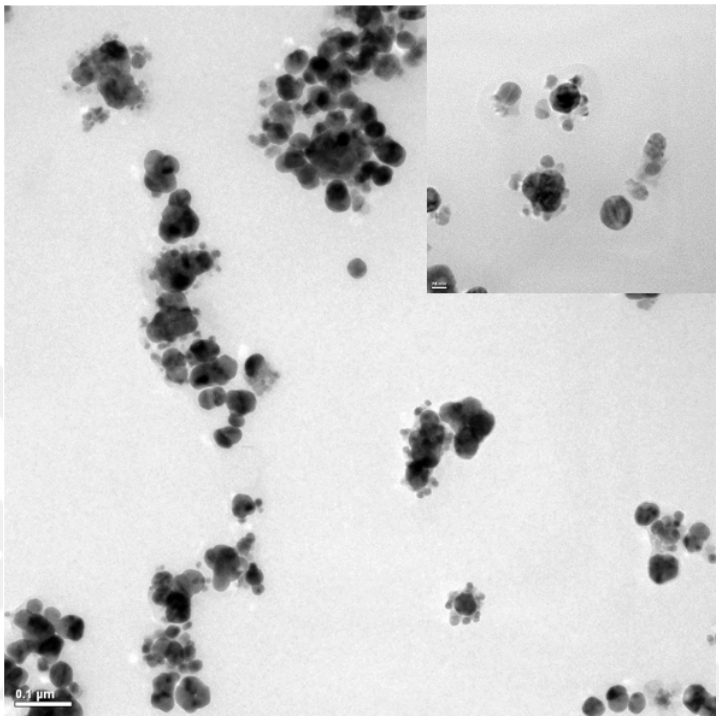

Figure 3.24: TEM image for Ag:Pd(1:1.3) NPs synthesized at 265 °C. Inset in the top right shows the Ag core-satellites and fusion of NPs.

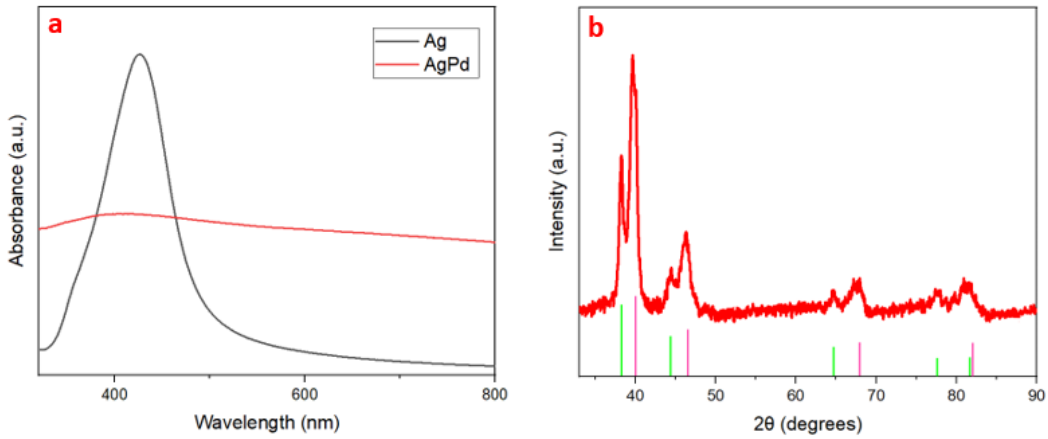

Figure 3.25: (a) UV-Vis spectra for AgPd core-satellite NPs synthesized at 265 °C and (b) X-ray diffraction pattern for Ag and AgPd, where green lines represent silver peaks and pink lines represent palladium peaks.

3.5 Ag-Pt Bimetallic Nanoparticles

3.5.1 Ag@AgPt Bimetallic Nanoparticles Synthesized @ 265 °C

Herein, Ag@AgPt NPs form at low platinum concentrations. Increasing platinum concentration in the reaction results in formation of alloyed Ag-Pt NPs, where the reaction is governed by galvanic replacement reaction. The final product to be obtained with GRR depends not only on the reduction potential of the metals but also on other parameters such as the kind of template used, type of solvent, temperature, etc [48].

This study used silver nanoparticles as core seed templates for platinum reduction at 265 °C. The solution's color turned brown, an indicator of platinum reduction. Platinum is known for its high reduction potential when compared to palladium [11]. $Pt(acac)_2$ served as the metal precursor, PVP as a capping agent, and DMF as a reducing agent. Different ratios of platinum/silver were attempted to form the bimetallic nanostructures.

Fig.3.26 shows the TEM images of the Ag@AgPt NPs synthesized at a ratio of (Ag: Pt = 1:2). The synthesized NPs exhibited an average particle size of 39.6 ± 4.2 nm (Fig.3.26d), around an average increase of 5 nm compared to the silver core nanoparticles. The galvanic replacement reaction occurred significantly when the platinum ratio was increased to 1:5 of silver to platinum. Platinum underwent galvanic replacement starting at each of the five edges of the five-folded twinned silver NPs. Increasing the platinum precursor to 1:5 of Ag: Pt resulted in further etching of the silver cores forming concave nano-cubes and nano-stars, where etching stops at the (111) planes [49] or closer ones, forming nano-stars as seen in Fig.3.27a-b.

STEM images (Fig.3.27c-d) show the distribution of Ag and Pt at (Ag:Pt = 1:5), which confirms the bimetallic formation. Silver and platinum exist in line

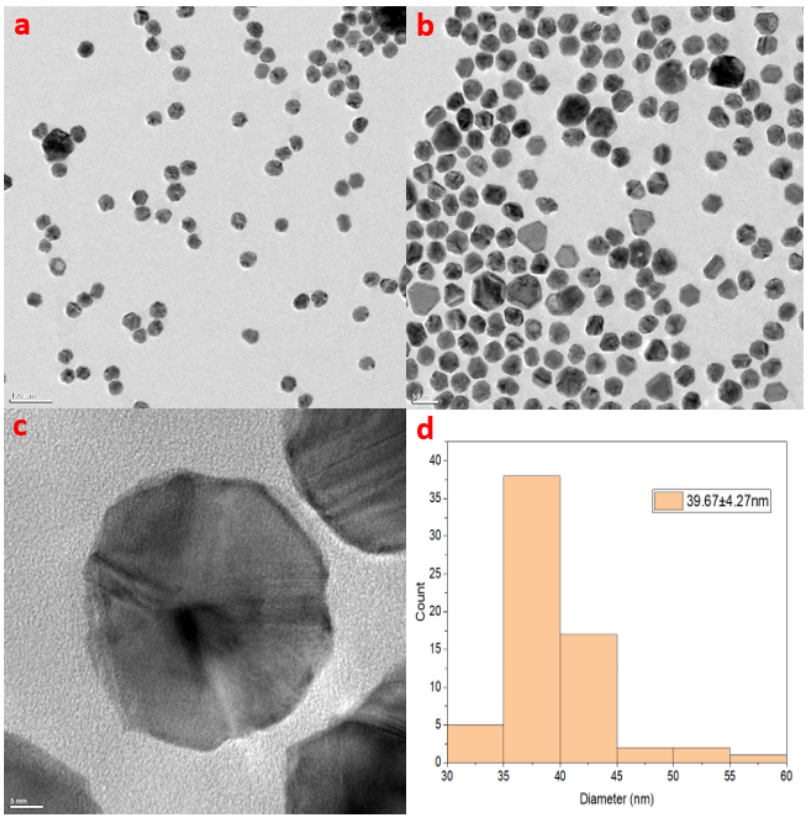

Figure 3.26: (a) Lower and (b) higher magnification TEM images for Ag:Pt(1:2) ratio, (c) HR-TEM image of a five-folded twinned Ag@AgPt nanoparticle. (d) size distribution for Ag:Pt(1:2) NPs. Scale bars are 100, 50, and 5 nm for a-c, respectively.

scan profile analysis, with silver more concentrated in the middle of the nanoparticle (Fig.3.27g). This result is confirmed with XRD analysis (Fig3.28b), where silver and alloy peaks exist, which concludes the formation of AgPt bimetallic NPs. The peaks of silver were all present in the Ag-Pt(1:2) at 38.20, 44.40, 64.60, 77.60, and 81.75° (JCPDS. no.04-0783). A peak at 39.50° starts to appear, shifting towards 39.80° as the platinum amount increases, corresponding to (111) planes of platinum [50]. The peaks of silver, at 44.40, 65.80, 77.60, and 81.75° broaden when increasing the amount of platinum, where this could be interpreted by the replacement of more of the silver content with platinum through the galvanic reaction and enhancement of the formation of an alloy [16]. This is related to lattice contraction due to the difference in sizes of Ag and Pt atoms [51]. This concludes the formation of bimetallic alloyed Ag-Pt NPs [52]. Size average starts

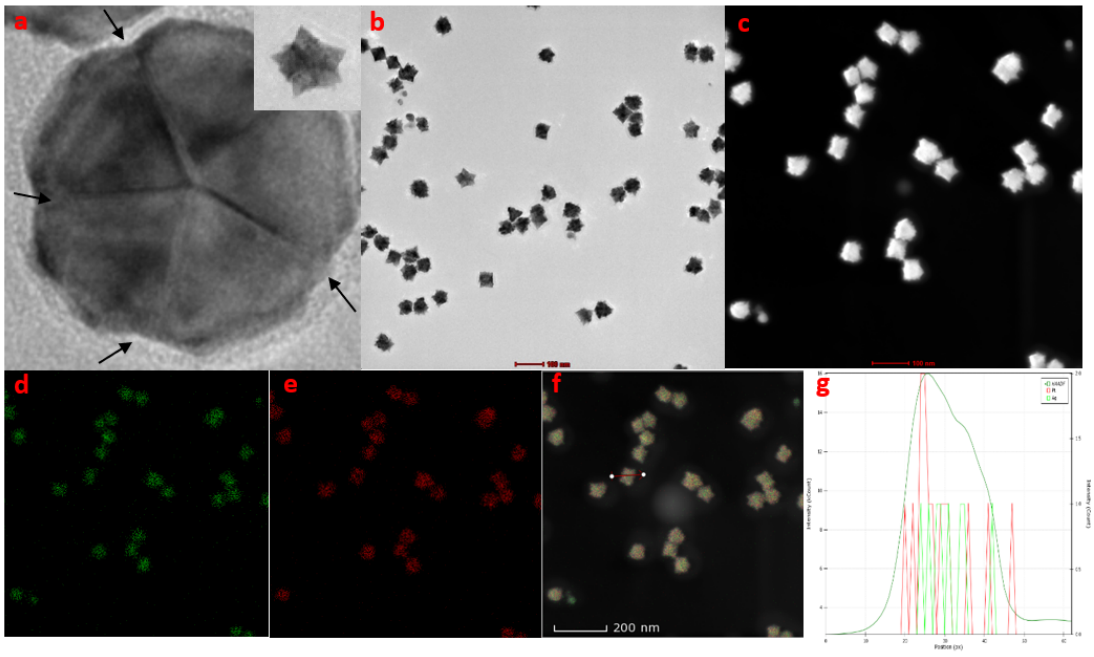

Figure 3.27: TEM images for (Ag:Pt= 1:5): (a) HR-TEM image for (Ag:Pt= 1:2) in comparison with the inset photo (Ag:Pt= 1:5), showing galvanic reaction starting at edges forming (111) planes shown as a nanostar. (b) bright-field TEM image showing concave cubes and nanostars, (c) dark-field TEM image of NPs, (d-f) STEM-HAADF-EDS images for silver (green), platinum (red) and the corresponding composition of both, respectively. (g) line-scan profile of a single NP. Scale bars are 100 nm for b-c, and 200 nm for d-f.

with Ag core NPs, where it increases with increasing platinum concentration: 34.6 ± 5.5, 49.3 ± 4.6, and 57.3 ± 6.2, corresponding to Ag, (Ag:Pt = 1:2), and (Ag:Pt = 1:5), respectively.

According to STEM images, it would be expected that if more platinum is fed into the reaction, a more homogeneous alloy would be formed with less silver remaining from the galvanic reaction and smaller size of the NPs due to galvanic replacement reaction. The d-spacing was calculated for the (Ag: Pt= 1:5) structure to be 0.229 nm and 0.234 nm, which correspond to AgPt and Ag (111) planes, respectively [53][54][55] (Fig.3.28a).

Fig.3.29 shows the results of analysis using UV-Vis spectroscopy. The LSPR

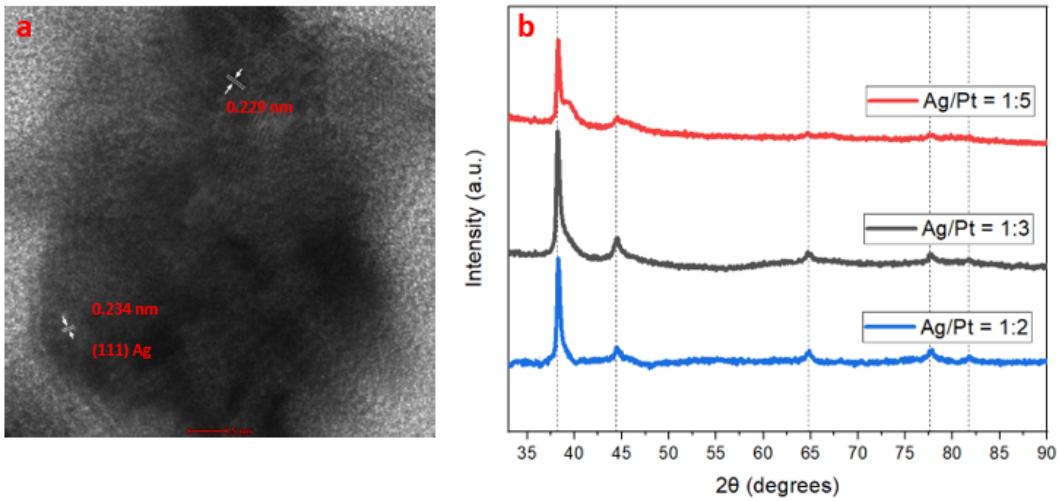

Figure 3.28: (a) HR-TEM showing the lattice spacing of (Ag:Pt= 1:5) structure, (b) X-ray diffraction (XRD) analysis of alloyed AgPt NPs at different ratios, synthesized at 265 °C.

peak blue-shifted from 426 nm (silver NPs) to 415, 405, and 396 nm, with increasing ratio of Pt: Ag to 2:1, 3:1 and 5:1, respectively. As platinum does not have a sharp LSPR like silver, the LSPR peak damps gradually when the platinum concentration is increased in the reaction and silver is etched.

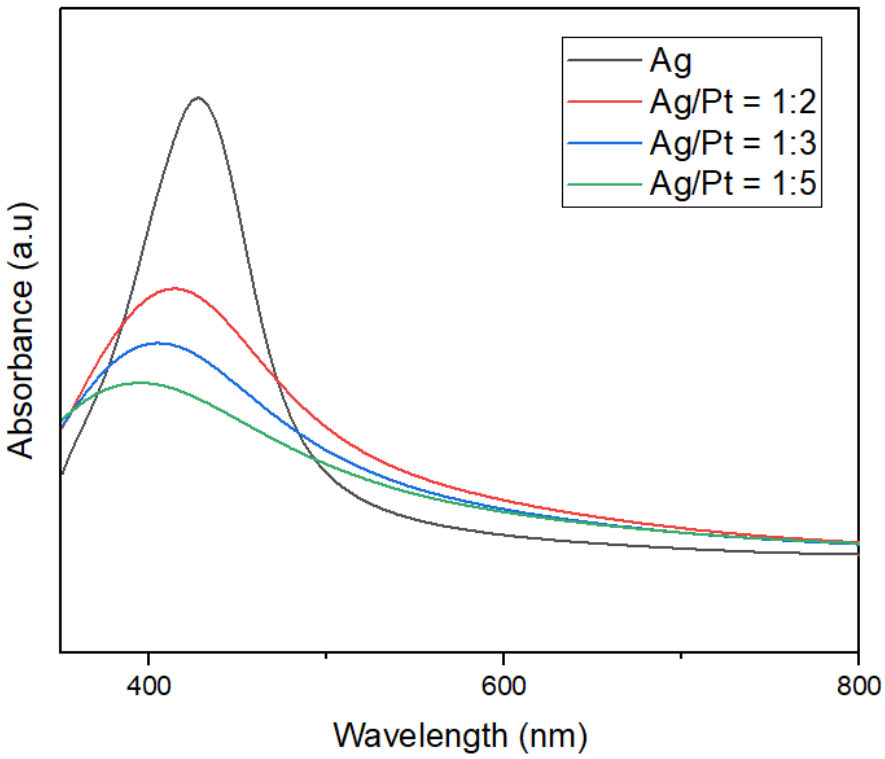

Figure 3.29: UV-Vis spectra of Ag@AgPt bimetallic NPs

3.5.2 Ag@AgPt Bimetallic Nanoparticles Synthesized @ 210 °C

In the previous section, platinum stabilized silver nanoparticles from forming satellites at 265 °C. Platinum is known to have a higher reduction potential than palladium. To prove the reduction potential efficiency of platinum at lower temperature, the reaction was attempted at 210 °C. Fig.3.30 shows that platinum stabilized silver NPs at 210 °C, with only a few NPs forming satellite structures.

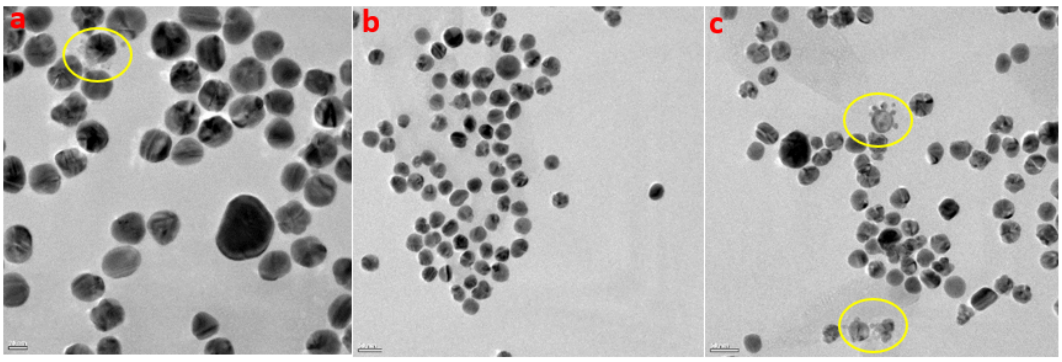

Figure 3.30: TEM images for (Ag:Pt = 1:2) synthesized at 210 °C at different magnifications (a-c), yellow circles show the Ag core-satellite formation

3.5.3 Ag-Pt Alloyed Bimetallic NPs synthesized @ 275 °C

In order to form fully alloyed Ag-Pt nanoalloys preventing galvanic reaction from taking place in etching such as the previous section, the reaction temperature was increased to 275 °C with (Ag:Pt= 1:4). Increasing the temperature by further 10 degrees allowed the silver core templates to get melted entirely down, where silver and platinum atoms are redistributed again creating a crystalline fcc structure with lattice distance of 0.229 nm corresponding to (111) AgPt alloyed NPs [53], forming a complete bimetallic nanoalloy. XRD shows peaks located between monometallic silver and platinum (silver peaks with reference from JCPDS no. 04–0783, and platinum peaks from the reference: JCPDS no. 04-0802, with an additional peak corresponding to (331) plane [56]. Fig.3.31 shows peaks of the AgPt alloy NPs at 39.20, 45.60, 66.50, 79.90, and 84.20°, where peaks are shifted more towards platinum due to the more platinum content in the alloy. A (1:4) ratio formed a full alloy at 275 °C and did not form an alloy at 275 °C with more platinum concentration. This suggests that 275 °C could be high enough to melt silver NPs in such a reaction environment.

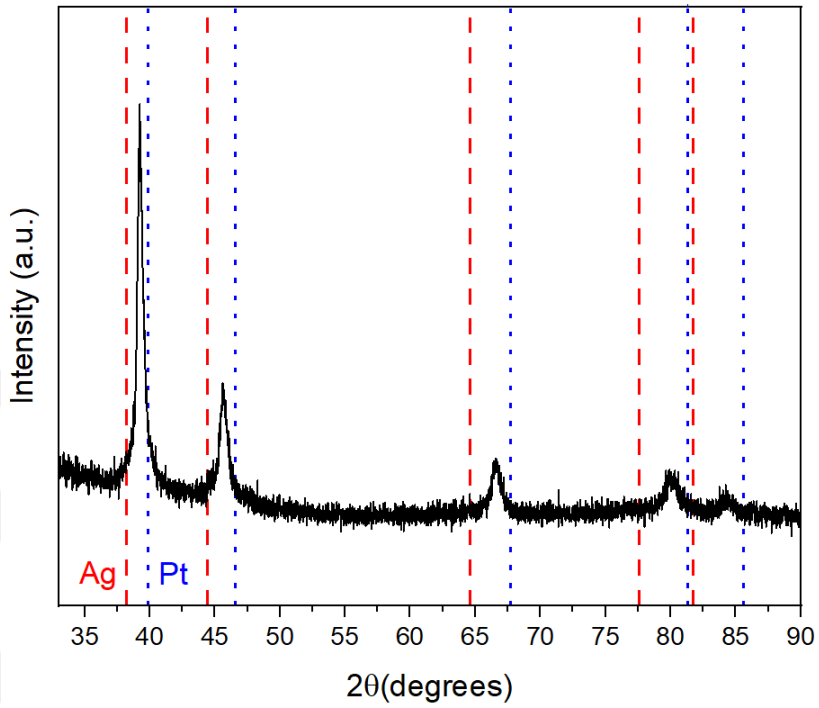

Figure 3.31: X-ray diffraction (XRD) analysis of AgPt(1:4) nanoalloy

3.6 AgPdPt Trimetallic NPs Synthesized @ 265 °C

Silver nanoparticles were used as base metals to reduce palladium and platinum, with a ratio of (Ag:Pd:Pt= 1:1.3:1.25). According to previous results, platinum should be reduced before palladium and stabilize silver cores. However, Fig.3.32b shows small satellites detached from core NPs, with a size of 18.1 ± 4 nm, more significant than the satellites' average size reported in the previous section. STEM analysis was investigated to explain further this phenomenon of satellite formation in the presence of platinum.

STEM images showed that palladium is uniformly distributed within the NPs (Fig.3.32), while platinum is more concentrated at the shell surface of NPs. This could indicate palladium reduction before platinum, where $Pd(acac)_2$ slows down

platinum reduction, allowing satellites to form. Palladium would then react with these silver NPs, forming an alloy; then platinum gets reduced on the shell, increasing the size of the satellites. This interpretation is supported with EDX analysis (Fig.3.32), where palladium content is higher than platinum in the nanoparticles.

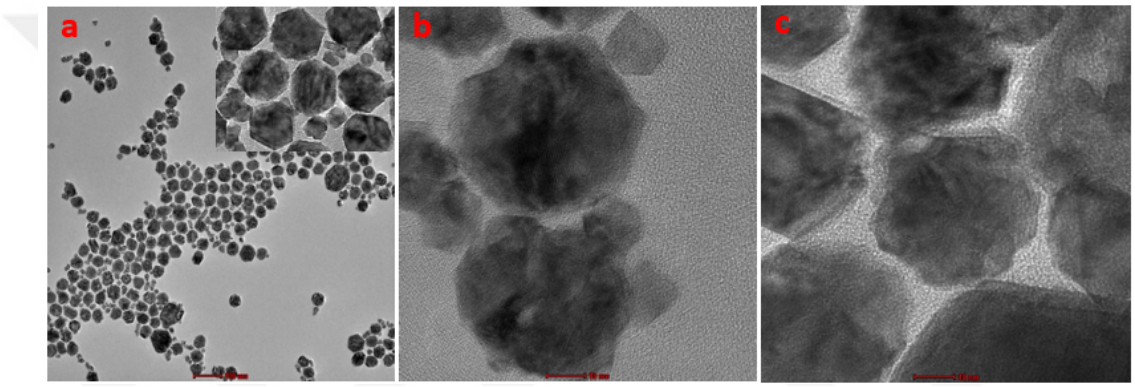

Figure 3.32: TEM images of trimetallic NPs synthesized at 265 °C (Ag:Pd:Pt = 1:1.5:1.25): (a) TEM image at a lower magnification with average size of core NPs of 45.3 ± 2.8 nm, the inset at the top right showing a higher magnification image showing the morphology nature of NPs synthesized, (b) TEM image showing satellite formation and (c) other nanoparticles without the core-satellite formation. Scale bars are 100, 10, and 10 nm for a-c.

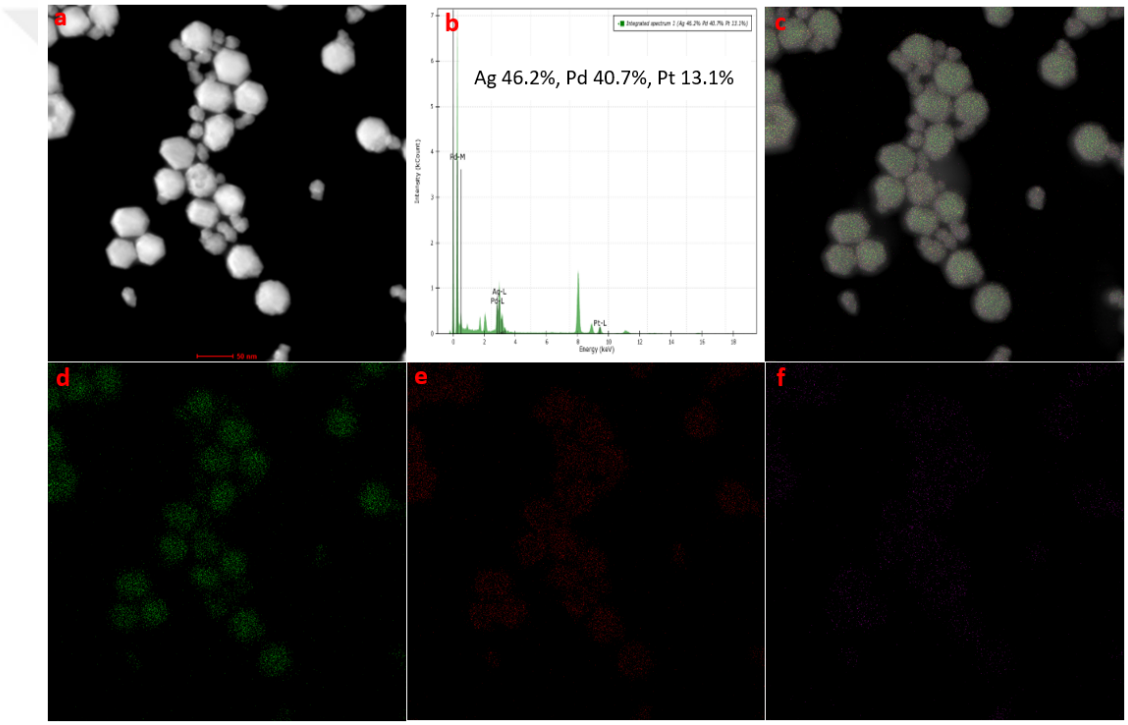

Figure 3.33: HAADF-TEM-EDX analysis for the trimetallic NPs: (a) dark-field TEM image, (b) EDX spectrum for the elemental composition of Ag, Pd, and Pt,(c) EDX elemental mapping showing the composition of Ag, Pd, and Pt, (d-f) EDX mapping for Ag(green), Pd(red), and Pt(pink), respectively. Scale bar is 50 nm for a,c, d-f.

Chapter 4

Conclusions

Bimetallic NPs of noble metals tend to have enhanced and more novel properties than their mono-metallic counterparts. Silver, a plasmonic metal, was synthesized in a facilitated green-synthesis method as a core seed or template for creating several nanostructures, including core-satellite, nanostars, NPs, and nanowires. Silver was reduced with PVP acting as a suitable dispersant and a capping agent, facilitating the reduction of silver acetylacetonate in water. In the synthesis of bimetallic NPs, silver acetylacetonate played several roles in the morphology of the NPs synthesized. Silver ions played a role in transforming palladium nanocubes into perfectly spherical NPs. Also, silver tended to undergo thermal decomposition, forming an Ag core-satellite structure, which allowed palladium to interact with silver, forming core-satellite Ag@AgPd. The selection of temperature was significant in determining the rate of satellite formation, where increasing the temperature to 265 °C yielded fusion of NPs and separate phases due to uncontrolled reaction.

Silver was also reduced on palladium nanocube seeds, forming bimetallic AgPd nanowires. In AgPt, platinum acted as a stabilizer, preventing silver from forming satellite structures at elevated temperatures. Silver was used as a template for galvanic replacement reaction with platinum at 265 °C. Increasing the platinum concentration facilitates the galvanic reaction, forming nanostars and concave

nanocubes. The selection of temperature was crucial in determining the type of reaction that proceeded, as increasing the temperature to 275 °C yielded an alloy instead of a galvanic replacement reaction. In addition, silver was used as a core for synthesizing trimetallic NPs, whereas palladium seemed to hinder platinum and allow the formation of silver satellites to be detached from the silver core.

Bibliography

[1] H. T. Nasrabadi, E. Abbasi, S. Davaran, M. Kouhi, and A. Akbarzadeh, "Bimetallic nanoparticles: Preparation, properties, and biomedical applications," *Artificial cells, nanomedicine, and biotechnology*, vol. 44, no. 1, pp. 376–380, 2016.

[2] M. Luo, Z. Zhao, Y. Zhang, Y. Sun, Y. Xing, F. Lv, Y. Yang, X. Zhang, S. Hwang, Y. Qin, *et al.*, "Pdmo bimetallene for oxygen reduction catalysis," *Nature*, vol. 574, no. 7776, pp. 81–85, 2019.

[3] G. Li, W. Zhang, N. Luo, Z. Xue, Q. Hu, W. Zeng, and J. Xu, "Bimetallic nanocrystals: Structure, controllable synthesis and applications in catalysis, energy and sensing," *Nanomaterials*, vol. 11, no. 8, p. 1926, 2021.

[4] A. Zaleska-Medynska, M. Marchelek, M. Diak, and E. Grabowska, "Noble metal-based bimetallic nanoparticles: the effect of the structure on the optical, catalytic and photocatalytic properties," *Advances in colloid and interface science*, vol. 229, pp. 80–107, 2016.

[5] J. W. Hong, S. W. Kang, B.-S. Choi, D. Kim, S. B. Lee, and S. W. Han, "Controlled synthesis of pd–pt alloy hollow nanostructures with enhanced catalytic activities for oxygen reduction," *ACS nano*, vol. 6, no. 3, pp. 2410–2419, 2012.

[6] K. Sytwu, M. Vadai, and J. A. Dionne, "Bimetallic nanostructures: combining plasmonic and catalytic metals for photocatalysis," *Advances in physics: X*, vol. 4, no. 1, p. 1619480, 2019.

[7] L. Yu, Q. Yan, and A. Ruzsinszky, "Key role of antibonding electron transfer in bonding on solid surfaces," *Physical Review Materials*, vol. 3, no. 9, p. 092801, 2019.

[8] R. Ferrando, J. Jellinek, and R. L. Johnston, "Nanoalloys: from theory to applications of alloy clusters and nanoparticles," *Chemical reviews*, vol. 108, no. 3, pp. 845–910, 2008.

[9] Z. Peng and H. Yang, "Designer platinum nanoparticles: Control of shape, composition in alloy, nanostructure and electrocatalytic property," *Nano today*, vol. 4, no. 2, pp. 143–164, 2009.

[10] N. Eom, M. E. Messing, J. Johansson, and K. Deppert, "General trends in core–shell preferences for bimetallic nanoparticles," *ACS nano*, vol. 15, no. 5, pp. 8883–8895, 2021.

[11] X. Huang, H. Zhang, C. Guo, Z. Zhou, and N. Zheng, "Simplifying the creation of hollow metallic nanostructures: one-pot synthesis of hollow palladium/platinum single-crystalline nanocubes," *Angewandte Chemie International Edition*, vol. 48, no. 26, pp. 4808–4812, 2009.

[12] J. Park, L. Zhang, S.-I. Choi, L. T. Roling, N. Lu, J. A. Herron, S. Xie, J. Wang, M. J. Kim, M. Mavrikakis, *et al.*, "Atomic layer-by-layer deposition of platinum on palladium octahedra for enhanced catalysts toward the oxygen reduction reaction," *ACS nano*, vol. 9, no. 3, pp. 2635–2647, 2015.

[13] S. Gao, S. Hao, Z. Huang, Y. Yuan, S. Han, L. Lei, X. Zhang, R. Shahbazian-Yassar, and J. Lu, "Synthesis of high-entropy alloy nanoparticles on supports by the fast moving bed pyrolysis," *Nature communications*, vol. 11, no. 1, p. 2016, 2020.

[14] M. A. Salem, E. A. Bakr, and H. G. El-Attar, "Pt@ ag and pd@ ag core/shell nanoparticles for catalytic degradation of congo red in aqueous solution," *Spectrochimica Acta Part A: Molecular and Biomolecular Spectroscopy*, vol. 188, pp. 155–163, 2018.

[15] Y. Yu, M. Li, Q. Li, J. Zhang, M. Sun, W. Qi, and J. Li, "Core-shell mgfe2o4@ c nano-composites derived via thermal decomposition-reduction dual strategy for superior lithium storage," *Journal of Alloys and Compounds*, vol. 834, p. 155207, 2020.

[16] V. Yadav, S. Jeong, X. Ye, and C. W. Li, "Surface-limited galvanic replacement reactions of pd, pt, and au onto ag core nanoparticles through redox potential tuning," *Chemistry of Materials*, vol. 34, no. 4, pp. 1897–1904, 2022.

[17] K. D. Gilroy, A. Ruditskiy, H.-C. Peng, D. Qin, and Y. Xia, "Bimetallic nanocrystals: syntheses, properties, and applications," *Chemical reviews*, vol. 116, no. 18, pp. 10414–10472, 2016.

[18] K. M. Koczkur, S. Mourdikoudis, L. Polavarapu, and S. E. Skrabalak, "Polyvinylpyrrolidone (pvp) in nanoparticle synthesis," *Dalton transactions*, vol. 44, no. 41, pp. 17883–17905, 2015.

[19] Z. Zhang, B. Zhao, and L. Hu, "Pvp protective mechanism of ultrafine silver powder synthesized by chemical reduction processes," *Journal of Solid State Chemistry*, vol. 121, no. 1, pp. 105–110, 1996.

[20] S. Giuffrida, G. Ventimiglia, and S. Sortino, "Straightforward green synthesis of "naked" aqueous silver nanoparticles," *Chemical communications*, no. 27, pp. 4055–4057, 2009.

[21] G. Merga, R. Wilson, G. Lynn, B. H. Milosavljevic, and D. Meisel, "Redox catalysis on "naked" silver nanoparticles," *The Journal of Physical Chemistry C*, vol. 111, no. 33, pp. 12220–12226, 2007.

[22] F. N. S. Neto, L. A. Morais, L. F. Gorup, L. S. Ribeiro, T. J. Martins, T. Y. Hosida, P. Francatto, D. B. Barbosa, E. R. Camargo, and A. C. Delbem, "Facile synthesis of pvp-coated silver nanoparticles and evaluation of their physicochemical, antimicrobial and toxic activity," *Colloids and Interfaces*, vol. 7, no. 4, p. 66, 2023.

[23] A. Mirzaei, K. Janghorban, B. Hashemi, M. Bonyani, S. G. Leonardi, and G. Neri, "Characterization and optical studies of pvp-capped silver nanoparticles," *Journal of Nanostructure in Chemistry*, vol. 7, pp. 37–46, 2017.

[24] N. A. C. Lah and S. Trigueros, "Synthesis and modelling of the mechanical properties of ag, au and cu nanowires," *Science and technology of advanced materials*, vol. 20, no. 1, pp. 225–261, 2019.

[25] M. Venkatesham, D. Ayodhya, A. Madhusudhan, A. Santoshi Kumari, G. Veerabhadram, and K. Girija Mangatayaru, "A novel green synthesis of silver nanoparticles using gum karaya: characterization, antimicrobial and catalytic activity studies," *Journal of Cluster Science*, vol. 25, pp. 409–422, 2014.

[26] J. C. Martínez Espinosa, R. Carrera Cerritos, M. A. Ramírez Morales, K. P. Sánchez Guerrero, R. A. Silva Contreras, and J. H. Macías, "Characterization of silver nanoparticles obtained by a green route and their evaluation in the bacterium of pseudomonas aeruginosa," *Crystals*, vol. 10, no. 5, p. 395, 2020.

[27] S. Elmegdar, R. Elkheloui, A. Laktib, R. Mimouni, and F. Hamadi, "Antibiofilm and anti-quorum sensing activities of biological nanoparticles," *Current applied acience and technology*, pp. e0257479–e0257479, 2023.

[28] H. Hieu, D. Trang, V. Hien, N. Nghia, N. Lam, and T. Nguyen, "Microorganism-mediated green synthesis of silver nanoparticles using aspergillus niger and bacillus megaterium," *Dig. J. Nanomater. Biostructures*, vol. 17, pp. 359–367, 2022.

[29] Y. Xia, Y. Xiong, B. Lim, and S. E. Skrabalak, "Shape-controlled synthesis of metal nanocrystals: simple chemistry meets complex physics?," *Angewandte Chemie International Edition*, vol. 48, no. 1, pp. 60–103, 2009.

[30] Y. Sun, B. Mayers, T. Herricks, and Y. Xia, "Polyol synthesis of uniform silver nanowires: a plausible growth mechanism and the supporting evidence," *Nano letters*, vol. 3, no. 7, pp. 955–960, 2003.

[31] N. Murshid and V. Kitaev, "Role of poly (vinylpyrrolidone)(pvp) and other sterically protecting polymers in selective stabilization of {111} and {100} facets in pentagonally twinned silver nanoparticles," *Chemical communications*, vol. 50, no. 10, pp. 1247–1249, 2014.

[32] Y. Xia, X. Xia, Y. Wang, and S. Xie, "Shape-controlled synthesis of metal nanocrystals," *Mrs Bulletin*, vol. 38, no. 4, pp. 335–344, 2013.

[33] H. T. Phan and A. J. Haes, "What does nanoparticle stability mean?," *The Journal of Physical Chemistry C*, vol. 123, no. 27, pp. 16495–16507, 2019.

[34] I. Pastoriza-Santos and L. M. Liz-Marzán, "N, n-dimethylformamide as a reaction medium for metal nanoparticle synthesis," *Advanced Functional Materials*, vol. 19, no. 5, pp. 679–688, 2009.

[35] A. Carone, S. Emilsson, P. Mariani, A. Désert, and S. Parola, "Gold nanoparticle shape dependence of colloidal stability domains," *Nanoscale Advances*, vol. 5, no. 7, pp. 2017–2026, 2023.

[36] X. Lin, S. Lin, Y. Liu, M. Gao, H. Zhao, B. Liu, W. Hasi, and L. Wang, "Facile synthesis of monodisperse silver nanospheres in aqueous solution via seed-mediated growth coupled with oxidative etching," *Langmuir*, vol. 34, no. 21, pp. 6077–6084, 2018.

[37] M. Zannotti, V. Vicomandi, A. Rossi, M. Minicucci, S. Ferraro, L. Petetta, and R. Giovannetti, "Tuning of hydrogen peroxide etching during the synthesis of silver nanoparticles. an application of triangular nanoplates as plasmon sensors for hg2+ in aqueous solution," *Journal of Molecular Liquids*, vol. 309, p. 113238, 2020.

[38] Q. Zhang, C. M. Cobley, J. Zeng, L.-P. Wen, J. Chen, and Y. Xia, "Dissolving ag from au- ag alloy nanoboxes with h2o2: A method for both tailoring the optical properties and measuring the h2o2 concentration," *The Journal of Physical Chemistry C*, vol. 114, no. 14, pp. 6396–6400, 2010.

[39] G. Blanco-Brieva, M. P. de Frutos Escrig, J. M. Campos-Martin, and J. L. Fierro, "Direct synthesis of hydrogen peroxide on palladium catalyst supported on sulfonic acid-functionalized silica," *Green Chemistry*, vol. 12, no. 7, pp. 1163–1166, 2010.

[40] Y.-J. Lee, N. B. Schade, L. Sun, J. A. Fan, D. R. Bae, M. M. Mariscal, G. Lee, F. Capasso, S. Sacanna, V. N. Manoharan, *et al.*, "Ultrasmooth, highly spherical monocrystalline gold particles for precision plasmonics," *ACS nano*, vol. 7, no. 12, pp. 11064–11070, 2013.

[41] J.-H. Huh, J. Lee, and S. Lee, "Comparative study of plasmonic resonances between the roundest and randomly faceted au nanoparticles-on-mirror cavities," *ACS Photonics*, vol. 5, no. 2, pp. 413–421, 2018.

[42] J. H. Yoon, F. Selbach, L. Schumacher, J. Jose, and S. Schlucker, "Surface plasmon coupling in dimers of gold nanoparticles: Experiment and theory for ideal (spherical) and nonideal (faceted) building blocks," *ACS Photonics*, vol. 6, no. 3, pp. 642–648, 2019.

[43] A. Brudzisz, D. Rajska, M. Gajewska, G. D. Sulka, and A. Brzózka, "Controlled synthesis and characterization of agpd nanowire arrays for electrocatalytic applications," *Journal of Electroanalytical Chemistry*, vol. 873, p. 114373, 2020.

[44] S. De Marchi, S. Núñez-Sánchez, G. Bodelón, J. Pérez-Juste, and I. Pastoriza-Santos, "Pd nanoparticles as a plasmonic material: synthesis, optical properties and applications," *Nanoscale*, vol. 12, no. 46, pp. 23424–23443, 2020.

[45] M. Kushwah, M. Gaur, A. N. Berlina, and K. Arora, "Biosynthesis of novel ag@ cu alloy nps for enhancement of methylene blue photocatalytic activity and antibacterial activity," *Materials Research Express*, vol. 6, no. 11, p. 116561, 2019.

[46] P. Han, P. Jin, X. Li, Y. Xu, K. Li, S. Wang, and Z. Nie, "Photoactivation of ambient oxygen via plasmon-coupled valence-band hybridization in agpd

nanoalloy for reaction pathway alteration," *Applied Catalysis B: Environmental*, vol. 298, p. 120598, 2021.

[47] Y. Hong, S. Venkateshalu, S. Jeong, G. M. Tomboc, J. Jo, J. Park, and K. Lee, "Galvanic replacement reaction to prepare catalytic materials," *Bulletin of the Korean Chemical Society*, vol. 44, no. 1, pp. 4–22, 2023.

[48] J. Chen, J. M. McLellan, A. Siekkinen, Y. Xiong, Z.-Y. Li, and Y. Xia, "Facile synthesis of gold- silver nanocages with controllable pores on the surface," *Journal of the American Chemical Society*, vol. 128, no. 46, pp. 14776–14777, 2006.

[49] Z. Li, Z. Xie, Y. Zhang, X. Mu, J. Xie, H.-J. Yin, Y.-W. Zhang, C. Ophus, and J. Zhou, "Probing the atomically diffuse interfaces in pd@ pt core-shell nanoparticles in three dimensions," *Nature Communications*, vol. 14, no. 1, p. 2934, 2023.

[50] X. Tan, S. Shahgaldi, and X. Li, "The effect of non-spherical platinum nanoparticle sizes on the performance and durability of proton exchange membrane fuel cells," *Advances in Applied Energy*, vol. 4, p. 100071, 2021.

[51] E. Fidiani, G. Thirunavukkarasu, Y. Li, Y.-L. Chiu, and S. Du, "Ultrathin agpt alloy nanorods as low-cost oxygen reduction reaction electrocatalysts in proton exchange membrane fuel cells," *Journal of Materials Chemistry A*, vol. 8, no. 23, pp. 11874–11883, 2020.

[52] V.-F. Ruiz-Ruiz, R. González-Olvera, R. Díaz-Pardo, I. Betancourt, I. Zumeta-Dubé, D. Díaz, N. Farfán, and M. J. Arellano-Jiménez, "Mechanochemically obtained pd–ag nanoalloys. structural considerations and catalytic activity," *Materialia*, vol. 4, pp. 166–174, 2018.

[53] X. Jiang, X. Yan, W. Ren, Y. Jia, J. Chen, D. Sun, L. Xu, and Y. Tang, "Porous agpt@ pt nanooctahedra as an efficient catalyst toward formic acid oxidation with predominant dehydrogenation pathway," *ACS Applied Materials & Interfaces*, vol. 8, no. 45, pp. 31076–31082, 2016.

[54] S. Some, B. Sarkar, K. Biswas, T. K. Jana, D. Bhattacharjya, P. Dam, R. Mondal, A. Kumar, A. K. Deb, A. Sadat, *et al.*, "Bio-molecule functionalized rapid one-pot green synthesis of silver nanoparticles and their efficacy toward the multidrug resistant (mdr) gut bacteria of silkworms (bombyx mori)," *RSC advances*, vol. 10, no. 38, pp. 22742–22757, 2020.

[55] X. Xiang, W. He, L. Xie, and F. Li, "A mild solution chemistry method to synthesize hydrotalcite-supported platinum nanocrystals for selective hydrogenation of cinnamaldehyde in neat water," *Catalysis Science & Technology*, vol. 3, no. 10, pp. 2819–2827, 2013.

[56] M. N. Kumar, B. Govindh, and N. Annapurna, "Green synthesis and characterization of platinum nanoparticles using sapindus mukorossi gaertn. fruit pericarp," *Asian J. Chem*, vol. 29, pp. 2541–2544, 2017.

[57] J. Yang, J. Yang, and J. Y. Ying, "Morphology and lateral strain control of pt nanoparticles via core–shell construction using alloy agpd core toward oxygen reduction reaction," *ACS nano*, vol. 6, no. 11, pp. 9373–9382, 2012.